

An Improved Estimate of the Coupled Arctic Energy Budget

MICHAEL MAYER,^{a,b} STEFFEN TIETSCHKE,^a LEOPOLD HAIMBERGER,^b TAKAMASA TSUBOUCHI,^c
JOHANNES MAYER,^b AND HAO ZUO^a

^a *European Centre for Medium-Range Weather Forecasts, Reading, United Kingdom*

^b *Department of Meteorology and Geophysics, University of Vienna, Vienna, Austria*

^c *Geophysical Institute, University of Bergen, Bergen, Norway*

(Manuscript received 29 March 2019, in final form 26 July 2019)


ABSTRACT

This study combines state-of-the-art reanalyses such as the fifth-generation European Re-Analysis (ERA5) and the Ocean Reanalysis System 5 (ORAS5) with novel observational products to present an updated estimate of the coupled atmosphere–ocean–sea ice Arctic energy budget, including flux and storage terms covering 2001–17. Observational products provide independent estimates of crucial budget terms, including oceanic heat transport from unique mooring-derived data, radiative fluxes from satellites, and sea ice volume from merged satellite data. Results show that the time averages of independent estimates of radiative, atmospheric, and oceanic energy fluxes into the Arctic Ocean domain are remarkably consistent in the sense that their sum closely matches the observed rate of regional long-term oceanic heat accumulation of $\sim 1 \text{ W m}^{-2}$. Atmospheric and oceanic heat transports are found to be stronger compared to earlier assessments (~ 100 and $\sim 16 \text{ W m}^{-2}$, respectively). Data inconsistencies are larger when considering the mean annual cycle of the coupled energy budget, with RMS values of the monthly budget residual between 7 and 15 W m^{-2} , depending on the employed datasets. This nevertheless represents an average reduction of $\sim 72\%$ of the residual compared to earlier work and demonstrates the progress made in data quality and diagnostic techniques. Finally, the budget residual is eliminated using a variational approach to provide a best estimate of the mean annual cycle. The largest remaining sources of uncertainty are ocean heat content and latent heat associated with sea ice melt and freeze, which both suffer from the lack of observational constraints. More ocean in situ observations and reliable sea ice thickness observations and their routinely assimilation into reanalyses are needed to further reduce uncertainty.

1. Introduction

The Arctic climate system is characterized by net energy loss to space throughout most of the year. Sustained poleward heat transports by atmosphere and ocean are required to balance this radiative imbalance (Peixoto and Oort 1992). In addition, there is a strong seasonality in the Arctic energy budget due to the strong seasonality of insolation, leaving an imprint on energy fluxes and storage. Thorough quantification of the long-term average, mean annual cycle, and trends of the Arctic energy budget is needed for improved process understanding and as reference data for model validation and development (Bourassa et al. 2013).

There exist numerous observation-based quantifications of the atmospheric energy budget of the Arctic (e.g., Nakamura and Oort 1988; Overland and Turet 1994; Semmler et al. 2005; Porter et al. 2010; Cullather and Bosilovich 2012). On the other hand, the ocean community has been focusing more on in situ based oceanic transport estimates through single straits into the Arctic Ocean [summarized in Dickson et al. (2008)], which recently have been synthesized using a consistent framework by Tsubouchi et al. (2018). Some assessments based on ocean reanalyses exist as well (e.g., Uotila et al. 2019), but there is an obvious lack of holistic estimates of the coupled Arctic energy budget. The study by Serreze et al. (2007), with some updates in Serreze and Barry (2014, hereafter SB14), seems to be an exception that provides estimates of the long-term mean and annual cycle of the coupled Arctic energy budget, including atmosphere, ocean, and sea ice. They relied on reanalyses and observations as much as

 Denotes content that is immediately available upon publication as open access.

Corresponding author: Michael Mayer, michael.mayer@ecmwf.int

DOI: 10.1175/JCLI-D-19-0233.1

© 2019 American Meteorological Society. For information regarding reuse of this content and general copyright information, consult the [AMS Copyright Policy \(www.ametsoc.org/PUBSReuseLicenses\)](https://www.ametsoc.org/PUBSReuseLicenses).

possible, but they used data sources that are now partly outdated, and their budget residual is large (see discussion below).

Improved estimates of the Arctic energy budget are essential to understand the pronounced warming trend in recent decades, which at the surface is stronger than the global average warming (Arctic amplification; Serreze and Barry 2011). Mayer et al. (2016) quantified the energy imbalance in the Arctic Ocean north of 70°N to be on the order of 1 W m^{-2} for the 2001–15 period, which is similar to the global average energy imbalance (see, e.g., Llovel et al. 2014). This implies that Arctic amplification is mainly confined to the surface, leaving a comparatively weak imprint on vertically integrated Arctic heat accumulation, which as a result is closer to the global mean than the Arctic surface warming. This is also suggested by results derived from coupled climate models (Burgard and Notz 2017).

From the standpoint of energy conservation, long-term mean net radiation at the top of the atmosphere (TOA) and the convergence of poleward atmospheric and oceanic energy transports into the Arctic must balance the regional heat accumulation. However, previous observational estimates are far from satisfying this requirement. For example, the estimates of mean net energy flux into the Arctic Ocean from the sum of atmospheric and oceanic lateral transports and net TOA radiation obtained by SB14 imply an unrealistic average energy loss of the system of 25 W m^{-2} . This inconsistency is clearly too large if the data are to be used for climate model validation.

Data paucity has been a major caveat of earlier estimates of the Arctic energy budget, hampering especially ocean and sea ice diagnostics. Surface properties of the latter two domains, such as sea ice concentration and sea surface temperature, are routinely observed by satellites. However, budget diagnostics additionally require exact knowledge of subsurface properties, such as sea ice thickness and vertically resolved ocean temperature. For example, SB14 made use of early-generation atmospheric reanalyses such as the 40-yr ECMWF Re-Analysis (ERA-40; Uppala et al. 2005), but their ocean and sea ice diagnostics had to rely on very sparse in situ data and low-resolution ocean model simulations.

In recent years, dynamical reanalyses have become available also for ocean and sea ice, and their quality and usefulness has been demonstrated in a number of studies (e.g., Balmaseda et al. 2015; von Schuckmann et al. 2018; Storto et al. 2019). Ocean–sea ice reanalyses still suffer from the data paucity in the Arctic, where observational constraints typically comprise remotely sensed

sea surface temperatures and sea ice concentrations and a relatively small number of in situ ocean profiles (Uotila et al. 2019), but it should be kept in mind that dynamical reanalyses are able to propagate information from data-rich into data-sparse regions and times (Balmaseda et al. 2013).

In terms of observations, several satellite-derived sea ice thickness datasets have become available over the past years, but their assimilation into analysis systems is only at its beginnings (Mu et al. 2018; Allard et al. 2018; Balan Sarojini et al. 2019). Another newly available and valuable data source is the mooring-derived oceanic transport dataset described in Tsubouchi et al. (2018). It compiles measurements from moored buoys located in Fram Strait, the Barents Sea Opening, Bering Strait, and Davis Strait in a mass-consistent way. This dataset thus represents a largely model-independent estimate of oceanic heat transports into the Arctic.

In the present study, we use state-of-the-art observational and reanalysis products to provide an updated and improved estimate of the long-term average and mean annual cycle of the coupled atmosphere–ocean–sea ice energy budget of the Arctic. A key advance with respect to earlier studies is the use of a budget framework that uses the same reference temperature across all compartments and thereby keeps ambiguities that result from unbalanced mass fluxes to a minimum (Mayer et al. 2017). The quality and consistency of the results are assessed by comparison to observation-based products wherever possible, and by a thorough examination of the budget residual, which will demonstrate the progress made compared to earlier works.

The rest of this paper is organized as follows. The diagnostic framework is presented in section 2, and data and study domain are described in section 3. The results are presented in section 4, which is subdivided into a description of the long-term mean budget (section 4a), the mean annual cycle (section 4b), and an assessment of budget closure (section 4c). A synthesis of the available data into a consistent best estimate of the mean annual cycle of all relevant budget terms is provided in section 5. Conclusions follow in section 6. A list of acronyms used throughout the text is provided in appendix C.

2. Diagnostic framework

We first discuss the vertically integrated energy budget equations for atmosphere, ocean, and sea ice—first separately and then how they can be combined to estimate the degree of budget closure.

For the total energy budget of the atmosphere we employ the simplified equation with three-dimensional moisture enthalpy fluxes consistently removed (introduced

error $< 1 \text{ W m}^{-2}$), but we retain the energetic effect of snowfall since this can be sizeable in high latitudes [see

Mayer et al. (2017) for derivation and detailed discussion]. The equation then reads as follows:

$$\begin{aligned} F_S &= \text{Rad}_{\text{TOA}} - \text{AET} - \nabla \cdot F_A + L_f(T_p)P_{\text{snow}} \\ &= \text{Rad}_{\text{TOA}} - \text{AET} - \frac{1}{g} \nabla \cdot \int_0^{p_s} [(1 - q_g)c_a(T_a - T_{00}) + L_v(T_a)q_g + \phi + k] \mathbf{v} dp + L_f(T_p)P_{\text{snow}}. \end{aligned} \quad (1)$$

Here, F_S is the net vertical energy flux (the sum of net surface radiation and turbulent fluxes) at the lower boundary of the atmosphere (land, sea ice, or open ocean) and is defined positive downward. Rad_{TOA} denotes net radiation at the top of the atmosphere (TOA), AET the atmospheric total energy tendency, $\nabla \cdot F_A$ the divergence of lateral atmospheric energy transports, g gravitational acceleration, p atmospheric pressure, q_g atmospheric water vapor content, T_a air temperature, T_{00} an arbitrary reference temperature (discussed below), c_a specific heat of dry air at constant pressure ($1003 \text{ J kg}^{-1} \text{ K}^{-1}$), L_v latent heat of vaporization ($2.501 \times 10^6 \text{ J kg}^{-1}$), ϕ geopotential, k kinetic energy, and \mathbf{v} the

horizontal wind vector. The snowfall term consists of latent heat of fusion $L_f(-0.3337 \times 10^6 \text{ J kg}^{-1})$ and snowfall rate P_{snow} (in $\text{kg m}^{-2} \text{ s}^{-1}$) and represents the cooling of the surface due to falling snow or, conversely, the additional latent heat release in an atmospheric column associated with net freezing (i.e., snow and ice that is not melted before reaching the surface). We assume that condensation and freezing occurs locally. Thus, Eq. (1) neglects lateral transports of liquid and frozen water in the atmosphere since these terms are very small.

The ocean vertically integrated sensible heat budget at a grid point with fractional sea ice cover f reads as follows:

$$\begin{aligned} fF_b + (1 - f)F_S &= \text{OHCT} + \nabla \cdot F_O - (1 - f)L_f(T_p)P_{\text{snow}} \\ &= \rho_0 c_p \frac{\partial}{\partial t} \int_0^Z (T_o - T_{00}) dz + \nabla \cdot \int_0^Z \rho_0 c_p (T_o - T_{00}) \mathbf{c} dz - (1 - f)L_f(T_p)P_{\text{snow}}. \end{aligned} \quad (2)$$

The net energy input at the top of the liquid ocean is the sum of basal heat flux F_b for the ice-covered fraction and F_S for the remaining fraction of the grid cell. It is balanced by the temporal tendency of ocean heat content (OHCT), the divergence of ocean heat transport ($\nabla \cdot F_O$), and the cooling effect of snowfall. In the explicit notation of OHCT and $\nabla \cdot F_O$, ocean temperature is denoted by T_o with a reference temperature T_{00} of -1.8°C (for reasons given below). Note that we

choose the same reference temperature T_{00} for both the ocean and the atmosphere. The ocean current vector is represented by \mathbf{c} . Seawater density ρ_0 (1026 kg m^{-3}) and specific heat of seawater c_p ($3990 \text{ J kg}^{-1} \text{ K}^{-1}$) are assumed constant. Vertical integration is then carried out using z coordinates from the surface to depth Z .

The sea ice heat budget at a grid point with fractional sea ice cover reads as follows:

$$\begin{aligned} fF_S - fF_b &\approx \text{MET} + \text{IHCT} + \nabla \cdot F_I + fM_{\text{snow}} \\ &= L_f \rho_i \frac{\partial d_i}{\partial t} + \rho_i c_i \frac{\partial [d_i (T_i - T_{00})]}{\partial t} + \nabla \cdot \rho_i d_i L_f \mathbf{c}_i + L_f \rho_{\text{snow}} \frac{\partial d_{\text{snow}}}{\partial t} - f L_f(T_p)P_{\text{snow}}. \end{aligned} \quad (3)$$

The left-hand side of Eq. (3) represents the vertical energy flux convergence into the sea ice. It is balanced by sea ice melt energy tendency MET (i.e., latent heat of fusion required and released during ice melt and freeze, respectively), sea ice sensible heat content tendency IHCT, the divergence of latent heat transport associated with sea ice $\nabla \cdot F_I$, and the energy required for snowmelt M_{snow} .

In the explicit notation of the terms of Eq. (3), ρ_i represents sea ice density (assumed constant at 928 kg m^{-3}), d_i gridpoint average sea ice thickness, c_i specific heat of sea ice ($2106 \text{ J kg}^{-1} \text{ K}^{-1}$), T_i sea ice temperature, \mathbf{c}_i the ice drift vector, ρ_{snow} snow density (assumed constant at 330 kg m^{-3} , in accordance with the setup of ORAS5), and d_{snow} gridpoint average snow thickness. Note that we neglect sensible heat contained in transported sea ice and

generally energetic effects of transported snow because they are very small in the context of this study.

As indicated earlier, we choose the freezing temperature of seawater as the reference temperature for all our calculations (i.e., $T_{00} = T_{\text{freeze}} = -1.8^\circ\text{C}$). The diagnostic advantage of this choice is that, although the liquid water volume in a column changes continuously due to freezing and melting of sea ice (Archimedes' principle), the OHC change associated with the volume change is zero since the lost/gained liquid water volume can be assumed to be at the seawater freezing temperature. At the same time, reference enthalpy of newly formed sea ice is zero, and thus no arbitrary heat appears in association with melting and freezing.

Equations (1)–(3) can be added to give the total energy budget for a coupled ocean–sea ice–atmosphere column:

$$\begin{aligned} \text{Rad}_{\text{TOA}} - \text{AET} - \nabla \cdot F_A &= \text{OHCT} + \nabla \cdot F_O + \text{MET} \\ &+ \text{IHCT} + \nabla \cdot F_I \\ &+ \text{MET}_{\text{snow}} + R. \end{aligned} \quad (4)$$

In Eq. (4), we combine the snowfall term from Eq. (1) with the snowmelt term from Eq. (2) to obtain the total latent heat tendency associated with changes in snow mass (MET_{snow}), which is the equivalent to MET. Given data imperfection and simplifications in the diagnostics, closure will not be perfect, and hence a budget residual R has been introduced in Eq. (4).

It is desirable to obtain a closed budget exclusively with physical terms (i.e., without a residual term). To achieve this, we choose a variational approach to enforce budget closure, following Mayer et al. (2014) and Mayer et al. (2018). The adjusted budget term F_k is computed following

$$F_k = F'_k + \frac{\sigma_k^2}{\sum_i \sigma_i^2} \sum_i F'_i, \quad (5)$$

where F'_k is the a priori estimate of the term, and σ_k^2 is the uncertainty of the respective budget term. Index i runs over all terms of the budget contained in Eq. (4). Thus, $\sum_i F'_i$ equals the budget residual R . Equation (5) basically distributes R across the physical budget terms according to their relative uncertainty. Practical implementation and specification of uncertainties will be described in section 5.

3. Data and study domain

Net radiation at TOA is taken from the Clouds and the Earth's Radiant Energy System–Energy Balanced

and Filled product (CERES-EBAF; Wielicki et al. 1996; Loeb et al. 2009) version 4.0 (Loeb et al. 2018). Atmospheric energy transports and storage are computed from the European Centre for Medium-Range Weather Forecasts (ECMWF) interim reanalysis (ERA-Interim; Dee et al. 2011) and the Japan Meteorological Agency (JMA) 55-year Re-Analysis (JRA-55; Kobayashi et al. 2015), as described in Mayer and Haimberger (2012) and Mayer et al. (2017). ERA-Interim and JRA-55 data used here cover 2001–17. We also present results from ECMWF's most recent atmospheric reanalysis ERA5, which includes several major technical improvements over ERA-Interim and a much enhanced spatial and temporal resolution (Hersbach et al. 2018). Our ERA5 diagnostics involve a number of technical improvements such as 1) vertical integration following the formulation of Simmons and Burridge (1981), 2) an iterative method to adjust the winds for mass inconsistencies that have been described, for example, in Mayer and Haimberger (2012), and 3) performance of all computations at hourly temporal and full T639 spatial resolution on a quadratic Gaussian grid to reduce aliasing, which will be described in detail elsewhere. Divergence fields from reanalyses are generally truncated to T63 to remove spectral noise, with the exception of ERA5, for which we show also fields at T180 (effectively 1°) resolution. We note that none of the employed reanalyses assimilates radiances measured from CERES instruments, and hence there is no interdependence between the TOA fluxes and any other physical budget terms presented here.

Ocean heat transport and ocean heat content are computed from the ECMWF ocean–sea ice reanalyses Ocean Reanalysis System 5 (ORAS5; Zuo et al. 2019), and the Centro Euro-Mediterraneo sui Cambiamenti Climatici (CMCC) Global Ocean Reanalysis System (C-GLORS) v5 and v7 (Storto and Masina 2016). ORAS5 and C-GLORS v7 cover 2001–17, and C-GLORS v5 2001–15. We also considered in situ based ocean heat content estimates from Hadley Centre EN4 (Good et al. 2013) but the strong seasonal dependence of data coverage did not allow for a meaningful assessment of the annual cycle. We additionally use observational estimates of ocean heat transport derived from moorings in the main Arctic Gateways within a mass-consistent framework (ARCGATE; Tsubouchi et al. 2018), covering 2005–09. Most of the mooring data ingested into ARCGATE are not assimilated in the employed ocean reanalyses, making this data product a largely independent source of information.

Sea ice volume and sea ice transport are computed from the above-mentioned ocean–sea ice reanalyses and the well-established sea ice reanalysis Pan-Arctic Ice

Ocean Modeling and Assimilation System (PIOMAS; Schweiger et al. 2011) version 2.1, covering also 2001–17. Snow terms and ice temperatures are taken from ORAS5. In addition to reanalysis information, we include remotely sensed sea ice thickness and volume from two satellite-based products. First, the *Ice, Cloud, and Land Elevation Satellite* (ICESat; Zwally et al. 2008; Kwok et al. 2009) retrieves ice thickness from laser altimetry, obtained over 15 missions during 2003–08. These missions (each covering time windows of approximately 34 days) can be categorized into fall (September–October), winter (February–March), and spring (May–June) missions. The three spring missions were not used because they involve large uncertainties associated with melting snow (R. Kwok 2019, personal communication). This left 12 missions for the present study. A second source of sea ice thickness data is the merged data product from *CryoSat2* and the Soil Moisture and Ocean Salinity satellites (henceforth CS2SMOS; Ricker et al. 2017), which provides weekly estimates of pan-Arctic sea ice thickness for the winter (October–March) months 2011–16. Neither ICESat nor CS2SMOS observations have been assimilated in the employed ocean reanalyses and hence can be used as fully independent products for validation.

Ocean and sea ice transports are computed on the native reanalysis grids at daily resolution. Instead of averaging divergence fields, we computed line integrals along the oceanic boundary of the study area (Pietschnig et al. 2018). Ocean heat content tendencies and sea ice tendencies are computed from snapshots or daily averages on the first of every month, depending on the data availability from the respective products. For CS2SMOS, weekly averages were first temporally interpolated to be centered on the first of the respective month before calculation of monthly tendencies.

Availability of ARCGATE data (2005–09) determines our main study period, but important diagnostics will also be provided for the longer 2001–17 period. The locations of the moorings in Bering Strait, Davis Strait, Fram Strait, and Barents Sea Opening define our main study area (see Fig. 1). Note that this is very similar to the Arctic Ocean domain used in SB14, with the exception that they excluded Baffin Bay, which however represents only a relatively small fraction of the total study area. Area averages throughout this paper will be given for the oceanic region bounded by the moorings. These area averages are indicated by curly brackets.

Several earlier studies provided budget estimates for the polar cap 70°–90°N. To facilitate comparison with those, we additionally provide results averaged over the polar cap (indicated by square brackets) in appendix A.

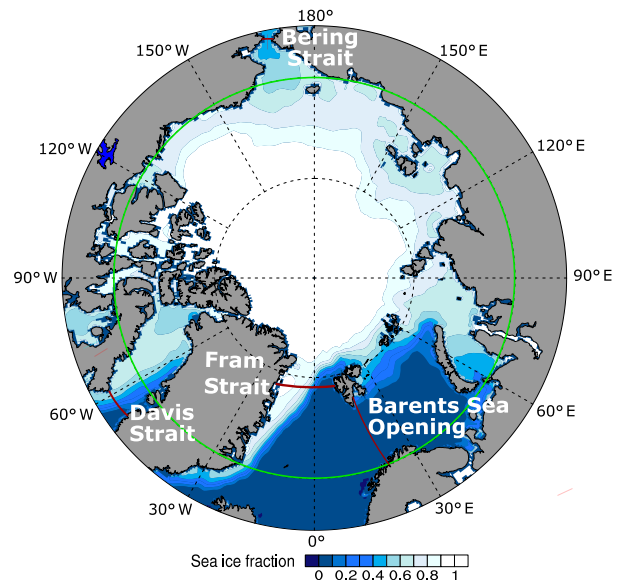


FIG. 1. Overview map of the main study area, which is the oceanic area bounded by the moorings in the Bering Strait, Davis Strait, Fram Strait, Barents Sea Opening (indicated by red lines; corresponds to $\sim 10.5 \times 10^6 \text{ km}^2$), and the polar cap (indicated by the 70°N latitude circle in green; corresponds to $\sim 14.8 \times 10^6 \text{ km}^2$). [Adopted from Pietschnig et al. (2018).]

4. Results

a. Long-term average energy budget

In this section, we provide new estimates of the long-term average fluxes of energy into the Arctic Ocean region and heat storage in this region, which manifest in ocean and atmosphere warming as well as ice melt. Heat storage estimates updated from Mayer et al. (2016) are presented in Fig. 2. The focus here is clearly on heat accumulation. A comprehensive assessment of ocean and sea ice mean states in reanalyses is provided, for example, by Uotila et al. (2019).

Ocean heat content accumulation for the top 300 m and the full ocean relative to the beginning of 2001 is presented in Fig. 2a. Long-term {OHC} increase is present in all three reanalyses. The agreement among the three products is good for the upper 300 m {OHC}, with similar long-term evolution and interannual variability. The latter reveals periods of enhanced heat uptake prior to the extreme September sea ice minima in 2007 and 2012 (when extensive open water susceptible to heat uptake was present in summer), and after 2015. Larger spread is present for full-depth {OHC}, with ORAS5 showing a stronger warming than C-GLORS v5 and v7 after 2010. The largest spread and lowest signal-to-noise ratio is found in the 300–700-m layer (not shown). The larger spread below 300 m indicates stronger model dependency of {OHC} because there are

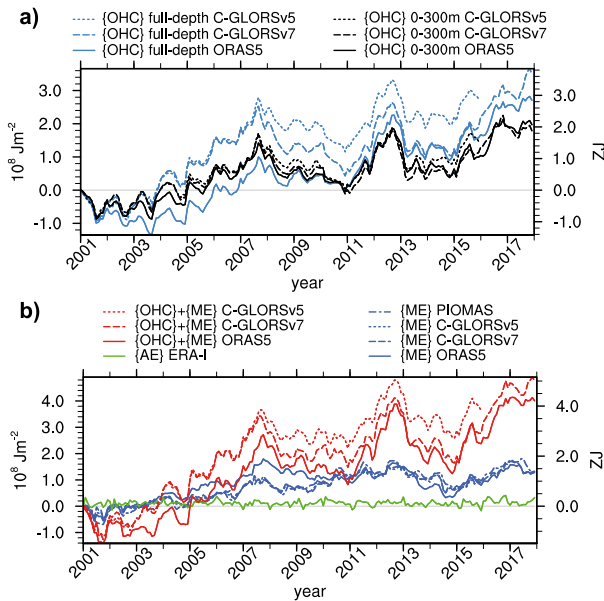


FIG. 2. (a) Full-depth and 0–300-m anomalous OHC and (b) melt energy (ME), atmospheric total energy, and ocean energy (OHC + ME) accumulation in the Arctic Ocean since 2001. The right axes indicate area-integrated values in zettajoules ($1 \text{ ZJ} = 10^{21} \text{ J}$).

hardly any in situ measurements, and the influence from assimilated SSTs is small.

The accumulated energy going into sea ice melting $\{\text{ME}\}$ from 2001–17 is presented in Fig. 2b. This term is about 50% smaller than the accumulated $\{\text{OHC}\}$ change. PIOMAS and C-GLORS v5 and v7 agree very well, which is no surprise given the fact that C-GLORS ice thickness is weakly relaxed toward PIOMAS ice thickness (Storto and Masina 2016). ORAS5 shows a stronger ice reduction in 2007 than the other products, but also a stronger recovery afterward. Over the full 2001–17 period, $\{\text{ME}\}$ increase is very similar in all products. Total ocean energy accumulation (full-depth $\{\text{OHC}\}$ plus $\{\text{ME}\}$) is mostly dominated by ocean heat content. It is interesting to note that ORAS5 has the strongest $\{\text{ME}\}$ increase but the weakest $\{\text{OHC}\}$ increase prior to 2007; that is, there seems to be large uncertainty about how the total ocean energy increase is partitioned between sea ice melt and ocean warming.

Atmospheric energy accumulation ($\{\text{AE}\}$; also shown in Fig. 2b) is small compared to the ocean and sea ice terms, reflecting the fact that the atmosphere absorbs only a small fraction of Earth’s energy imbalance (Von Schuckmann et al. 2016).

We convert energy accumulation shown in Fig. 2 to rates of change (i.e., tendencies), using the Theil–Sen median-of-pairwise-slopes trend estimator (Sen 1968). Results are summarized in Table 1. The total ocean warming rate ($=\{\text{OHCT}\} + \{\text{MET}\}$) is around 1 W m^{-2} for the period 2001–17, of which $\sim 1/3$ is attributable to sea ice melt. AET is negligible. Values are similar for the shorter 2005–09 period, albeit with larger spread. Overall, these results are very similar to those presented in Mayer et al. (2016). As already noted from the time series in Fig. 2, relative discrepancies are larger for $\{\text{OHCT}\}$ and $\{\text{MET}\}$ than for their sum.

We now turn to the long-term average of energy fluxes into the study area. To facilitate comparison to the ARCGATE data, 2005–09 averages are provided in Table 2. On average, there is a strong energy loss at TOA of -115.8 W m^{-2} , which is balanced by lateral heat transports in the ocean and the atmosphere. Average atmospheric energy convergence is in the range of 95.7 to 98.7 W m^{-2} . Reanalysis-based ocean heat transport into the Arctic ranges from 11.3 to 13.4 W m^{-2} , whereas observation-based heat transport from the ARCGATE data is stronger (14.8 W m^{-2}). Latent heat transport into the study area through ice export ranges from 1.1 to 2.0 W m^{-2} . This transport is positive into the Arctic, as the exported sea ice carries lower values of energy (reduced by latent heat of freezing) than the inflowing liquid water replacing it. Although these values are small, the large relative spread between the products suggests large uncertainties in reanalyzed sea ice thickness.

From an energy conservation standpoint, energy accumulation results from an imbalance of energy fluxes into the study area; that is, there is stronger energy input than loss (von Schuckmann et al. 2016). Thus, the degree of agreement between values in Tables 1 and 2 is a measure of data consistency. Taking all possible combinations of flux data, we obtain a total energy input ($=\{\text{Rad}_{\text{TOA}}\} - \{\nabla \cdot F_A\} - \{\nabla \cdot F_O\} - \{\nabla \cdot F_I\}$) in the range of -7.7

TABLE 1. 2005–09 (2001–17 values shown in parentheses) rates of change in the three main storage terms averaged over the Arctic Ocean; units are W m^{-2} (conversion factor to obtain TW is 10.51). The asterisk denotes 2001–15 values.

	$\{\text{OHCT}\}$	$\{\text{MET}\}$	$\{\text{OHCT}\} + \{\text{MET}\}$	$\{\text{AET}\}$
ORAS5	0.62 (0.65)	0.45 (0.24)	1.07 (0.90)	—
C-GLORS v7	0.30 (0.55)	0.29 (0.31)	0.54 (0.85)	—
C-GLORS v5	0.83 (0.91*)	0.33 (0.42*)	1.11 (1.30*)	—
PIOMAS	—	0.40 (0.36)	—	—
ERA-Interim	—	—	—	0.01 (−0.02)

TABLE 2. 2005–09 (2001–17 values shown in parentheses) mean energy fluxes into the study area; units are W m^{-2} (conversion factor to obtain TW is 10.51). The asterisk denotes 2001–15 values.

	$\{\text{Rad}_{\text{TOA}}\}$	$-\{\nabla \cdot F_A\}$	$\{F_S\}_{\text{implied}}$	$-\{\nabla \cdot F_O\}$	$-\{\nabla \cdot F_I\}$
CERES-EBAF 4.0	-115.8 (-116.3)	—	—	—	—
ERA-Interim	—	98.3 (98.0)	-17.5 (-18.3)	—	—
JRA-55	—	95.7 (96.0)	-20.0 (-20.3)	—	—
ERA5	—	98.7 (98.6)	-17.0 (-17.7)	—	—
ORAS5	—	—	-14.5 (-13.3)	13.4 (12.5)	2.0 (1.9)
C-GLORS v7	—	—	-13.2 (-13.0)	12.6 (12.2)	1.4 (1.3)
C-GLORS v5	—	—	-11.4 (-11.0)	11.3 (11.0*)	1.1 (1.1*)
ARCGATE	—	—	-15.7 ^a (-)	14.8 (-)	—
PIOMAS	—	—	—	—	1.8 (1.6)
SB14	-115	84	-31	3	3

^a This value is based on a combination of ARCGATE ocean heat and ORAS5 ice transport estimates. SB14 values are based on various periods, mainly before the 2000s.

to -0.3 W m^{-2} . This means that the sum of the fluxes into the Arctic is generally too small to balance the observed storage rate, where the combination of CERES/ERA5/ARCGATE/ORAS5 is closest to achieving a balanced budget with a total energy input of -0.3 W m^{-2} . Results are very similar when considering the full 2001–17 period.

Budget inconsistencies also show up when comparing inferred net surface energy flux from either the atmospheric energy budget [Eq. (1)] or the ocean and sea ice budget [Eqs. (2) and (3)]. From the atmospheric budget we obtain an $\{F_S\}$ estimate in the range of -17.0 to -20.0 W m^{-2} , while the $\{F_S\}$ estimate from the ocean side ranges between -11.4 and -15.7 W m^{-2} , with the strongest negative value derived from ARCGATE-based ocean heat transports (see values in Table 2). The non-overlap of these two ranges is a sign of nonclosure in the coupled budget.

These results can be compared to an earlier assessment by SB14, shown in Table 2 as well. Discussion of discrepancies with our results can be found in section 5. Here we only note that the sum of their flux and storage estimates amounts to -20 W m^{-2} , which represents a much more severe imbalance than that obtained from our results.

Since many earlier studies provided results for the polar cap north of 70°N , we present estimates for the polar cap as well (see appendix A). Results are largely similar to those for the Arctic Ocean domain. One salient difference from the Arctic Ocean domain results is the higher total ocean warming rates in the range of 1.1 to 1.6 W m^{-2} with regard to the oceanic area north of 70°N (based on 2001–17 estimates in Table A1). The additional warming is mainly located in the North Atlantic (not shown), but this seems to be related to decadal variability related to the North Atlantic Oscillation and meridional overturning circulation (Robson et al. 2012). Another feature of the results in appendix A

is the slightly larger discrepancies in inferred surface energy fluxes from either the atmospheric or oceanic budget (see values in Table A2), likely because we do not have in situ based oceanic transports (which are deemed more reliable than those from reanalyses) available for this region.

b. Quantification of the mean annual cycle

The mean annual cycle of the main budget terms in Eqs. (1)–(3) averaged over 2005–09 is presented in Fig. 3. The spread between the estimates from different products, defined as maximum minus minimum estimate in the respective month, is presented in Fig. 4.

Atmospheric fluxes and storage are presented in Fig. 3a. Net radiation at TOA exhibits a pronounced annual cycle which is mainly driven by solar radiation. It is mostly negative except for June and July when solar insolation is at its maximum. A large fraction of $\{\text{Rad}_{\text{TOA}}\}$ is balanced by the convergence of lateral atmospheric energy transports. The annual cycle of $-\{\nabla \cdot F_A\}$ is sizeable, ranging from $\sim 123 \text{ W m}^{-2}$ in January to $\sim 80 \text{ W m}^{-2}$ in March–August. The agreement between JRA-55, ERA-Interim, and ERA5 is good with a maximum spread of 11 W m^{-2} in July, providing high confidence in the quantification of this term. The annual cycle of atmospheric energy storage is moderate, with a maximum of $\sim 26 \text{ W m}^{-2}$ in April and a minimum of $\sim -27 \text{ W m}^{-2}$ in September. Implied net surface energy flux exhibits a strong annual cycle, which is mainly governed by net radiation at TOA.

Figure 3b shows the annual cycle of ocean heat transport and latent heat transport associated with sea ice transport. All $-\{\nabla \cdot F_O\}$ estimates exhibit an annual cycle with maximum ocean heat transports during September–January and minimum ocean heat transports during April–June. Results from ocean reanalyses are very similar and generally agree favorably with

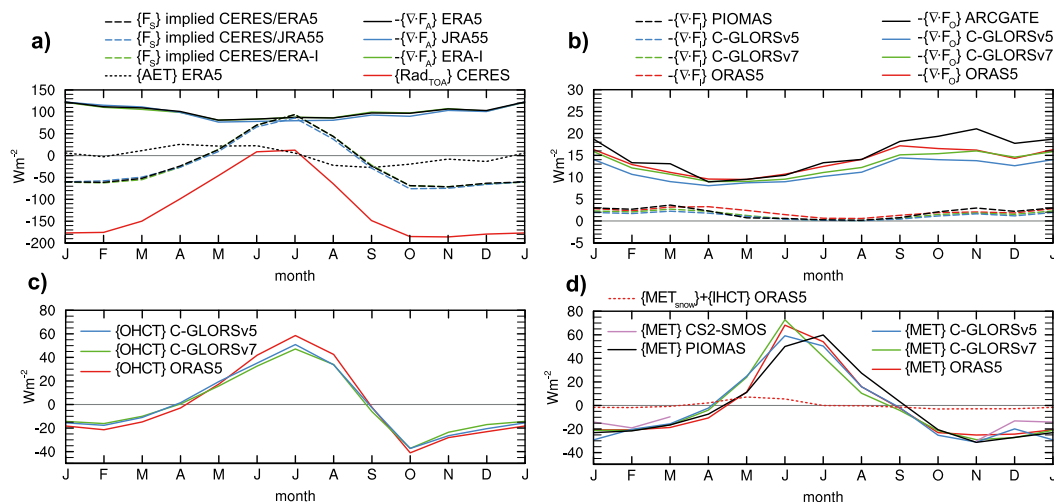


FIG. 3. Mean annual cycle (2005–09) of the main terms of the coupled Arctic energy budget (Arctic Ocean area averages): (a) atmospheric terms, (b) convergence of ocean heat transport and ice latent heat transport, (c) full-depth ocean heat content tendency, and (d) melt energy tendency (MET) and the sum of sea ice sensible heat (IHCT; from ORAS5) and latent heat stored in snow on ice (MET_{snow} ; from ORAS5).

observations from ARCGATE, except for November–January, when ARCGATE values are higher than the reanalysis-based estimates and spread reaches $\sim 7 \text{ W m}^{-2}$ (see Fig. 4). As already seen from the long-term average (see Table 2), latent heat transport associated with sea ice is generally small in magnitude (Fig. 3b). Ice export is largest in late winter and goes to zero in summer in all products except for ORAS5. The spread among the products is relatively large throughout the year.

Figure 3c shows the annual cycle of $\{\text{OHCT}\}$ from three ocean reanalyses. The general picture of relatively sharp summer warming peaking at around $50\text{--}60 \text{ W m}^{-2}$ in July (when also the spread peaks at $\sim 12 \text{ W m}^{-2}$; see Fig. 4) and a broader winter cooling with a more modest minimum of $\sim -40 \text{ W m}^{-2}$ in October is the same for all three products. $\{\text{OHCT}\}$ from ORAS5 exhibits the most pronounced seasonal cycle.

The annual cycle of $\{\text{MET}\}$ is presented in Fig. 3d. Compared to $\{\text{OHCT}\}$, the spread is larger for this term and peaks in June at $\sim 23 \text{ W m}^{-2}$, when values range from ~ 50 to more than 70 W m^{-2} . Moreover, the timing of maximum melt is different in the products (June in ORAS5, C-GLORS v5 and v7, July in PIOMAS). Ice melt and freeze in PIOMAS seem generally delayed compared to the other products, which might be related to the different approach to sea ice concentration assimilation in this product (Lindsay and Zhang 2006). Also shown in Fig. 3d is November–March $\{\text{MET}\}$ derived from CS2SMOS, which indicates substantially weaker freezing than all other products during December–March and thereby increases the spread

during winter (see Fig. 4). Note that the CS2SMOS results represent a 2011–16 average, but reanalysis results are very similar for this period (not shown). The $\{\text{MET}\}$ discrepancies will be investigated further in section 4c(3).

The sum of $\{\text{IHCT}\}$ and $\{\text{MET}_{\text{snow}}\}$ is not negligible. It peaks at $\sim 8 \text{ W m}^{-2}$ in May–June, when sea ice warming and snowmelt are at their maximum, representing about 10% of the main ocean storage terms $\{\text{OHCT}\}$ and $\{\text{MET}\}$. Consequently, we include these terms in the assessments of budget closure following in the next section.

c. Assessment of budget closure

In this section we assess the realism and degree of closure of the results presented in section 4a and section 4b from various perspectives. Satisfaction of physical constraints and validation against observation-based

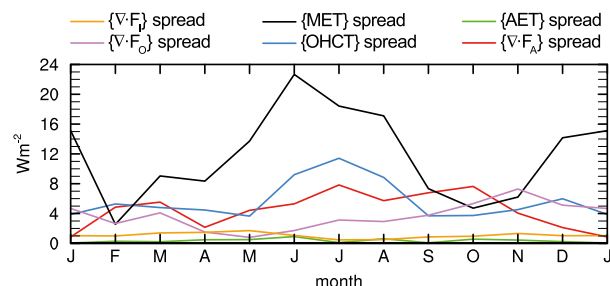


FIG. 4. Mean annual cycle (2005–09) of spread in estimates of different energy budget terms, computed as respective maximum minus minimum estimate provided in Figs. 3a–d.

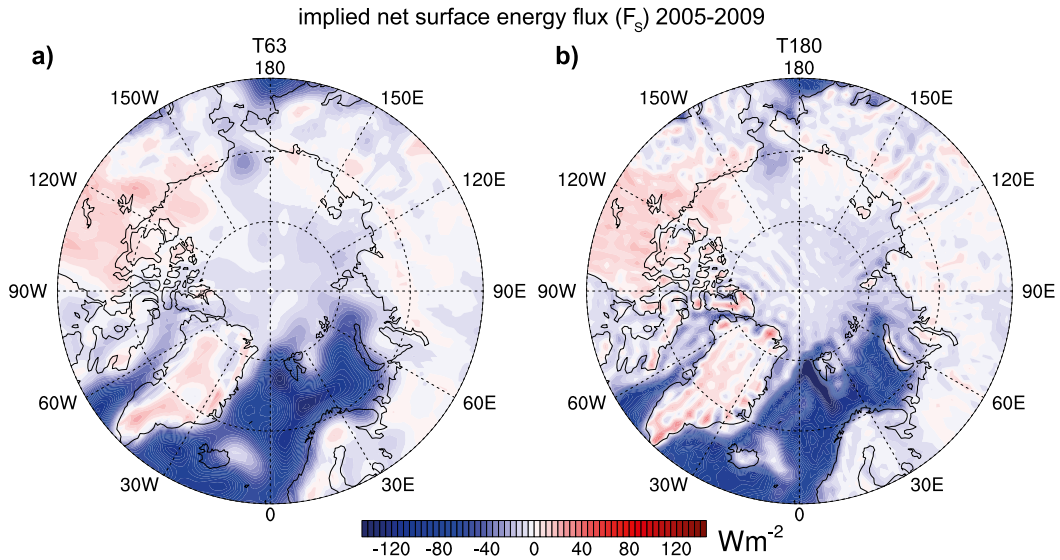


FIG. 5. Mean implied F_S (2005–09) using CERES-EBAF net TOA fluxes and atmospheric transports from ERA5 truncated at (a) T63 and (b) T180. Units are W m^{-2} and positive values denote a downward net flux.

data will help to pinpoint the largest sources of uncertainty in our assessment.

1) YEARLY-MEAN IMPLIED NET SURFACE ENERGY FLUX

We infer 2005–09 average inferred net surface energy flux as evaluated from the right-hand side of Eq. (1), using CERES-EBAF net TOA radiation and atmospheric energy transports from the different used reanalysis products. Figure 5 presents results based on ERA5 data at T63 and T180 resolution. They show realistic large-scale patterns, with strong fluxes out of the ocean in the North Atlantic and low values elsewhere. However, results truncated at T63 (Fig. 5a) do not reproduce the sharp gradients across the ice edge and coast lines very well, which are much clearer in the ERA5 results truncated at T180 (Fig. 5b). The higher resolution also brings out very clearly the prominent local minimum in air–sea fluxes in the Icelandic Sea that has been documented by Moore et al. (2012). However, it is evident that at T180 some spectral noise creeps in as well. The air–sea heat flux along the ice edge plays a vital role in open ocean deep convection in Greenland and Iceland Seas that contributes to Denmark Strait overflow water (Moore et al. 2015; Brakstad et al. 2019). The ERA5-derived surface fluxes at T180 depict the imprint of these processes at a high level of detail, which is remarkable given that this is an indirect estimate of F_S . However, also the relatively high-resolution result is not able to reproduce the imprint of ocean heat loss associated with the sea ice production along the Siberian

coast, which is due to the fact that ERA5 assumes constant sea ice thickness of 1.5 m and thus sees far too weak air–sea flux through the thin ice actually present in this region (Tietsche et al. 2018).

A more quantitative quality assessment of inferred F_S is to look over land, where the long-term average should be fairly small. In the steady state (denoted by the overbar), average F_S over land should balance the average energy going into snowmelt (on the order of $2\text{--}3 \text{ W m}^{-2}$ locally on an annual mean basis; see Liu et al. 2015; Mayer et al. 2017) when neglecting long-term land (sub)surface warming and warming of surface waters discharged later:

$$\overline{F_{S,\text{land}}} = \overline{M_{\text{snow,land}}} = -\overline{L_f(T_p)P_{\text{snow}}}. \quad (6)$$

Land averages of inferred F_S range from -4.4 (ERA-Interim, not shown) to -1.2 W m^{-2} (JRA-55; not shown), that is, too low values, indicating too weak poleward energy transports from subarctic regions or too weak ocean-to-land energy transports in the reanalyses or too weak radiative energy input at TOA. In terms of noise, the ERA5-based result at T63 (T180) performs best with an RMS value of 11.8 (11.1) W m^{-2} over land, compared to results of 12.1 W m^{-2} from ERA-Interim and 15.8 W m^{-2} from JRA-55. A composite of the three estimates (based on ERA5, ERA-Interim, and JRA-55) at T63 brings the RMS value down to 11.6 W m^{-2} . Generally, our inferred F_S fields seem much smoother compared to earlier results, such as those shown by Porter et al. (2010).

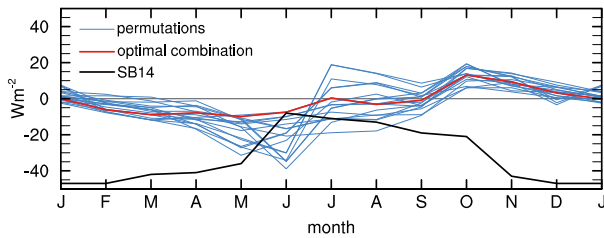


FIG. 6. Mean annual cycle of different realizations (“permutations” in blue) of the budget residuals $\{R\}$ (as described in the main text) and the optimal combination yielding the smallest RMS value (red; see text for explanation). Results based on values in SB14 are shown as well (black).

2) BUDGET RESIDUAL OF THE MEAN ANNUAL CYCLE

Here we use Eq. (4) to evaluate the residual R of the mean annual cycle of the coupled atmosphere–ocean–sea ice budget. To explore the residual resulting from the use of different input datasets, we compute R using all meaningful combinations of data. For example, one combination is CERES-EBAF for Rad_{TOA} ; ERA-Interim for $\nabla \cdot F_A$ and AET; ORAS5 for OHCT, MET, IHCT, $\nabla \cdot F_I$, and MET_{snow} ; and ARCGATE for $\nabla \cdot F_O$. Possible permutations are to exchange, for example, ERA-Interim with JRA-55 data, or ORAS5 with CGLORSv7 data. Two of the terms can be derived from reanalyses, but also exclusively from observational data: Rad_{TOA} from CERES-EBAF and $\nabla \cdot F_O$ from ARCGATE. There are good reasons to assume that observational estimates for these terms are superior to any reanalysis estimates, so we always use the observational estimates. Because the interproduct spread in $\nabla \cdot F_I$ is small (see Fig. 3b), we always use the ensemble mean computed from the four ocean–sea ice reanalyses. With three atmospheric reanalyses, three ocean–sea ice reanalyses and one sea ice-only (PIOMAS) reanalysis, the latter of which is combined with OHC data from the three other reanalyses, we can thus obtain 18 different permutations of input data and consequently 18 realizations of the budget residual R .

Figure 6 shows the mean annual cycle of $\{R\}$ using the 18 combinations of input data described above. The values of the different permutations range within $\pm 15 \text{ W m}^{-2}$ during most of the year but can reach extreme values between -38.9 and 19.3 W m^{-2} in summer, when also the spread between the different permutations is largest. The strongest negative values are attained in June by permutations that use ORAS5 and CGLORSv7 data. Note that these reanalyses also exhibit the highest $\{\text{MET}\}$ values in June (cf. Fig. 3d). The absolute value of all estimates of $\{R\}$ reaches another maximum in October, when ocean storage rates are

most negative (cf. Figs. 3c and 3d). This suggests that the annual cycle of ocean energy storage (the sum of OHCT and MET) is exaggerated in our datasets, which will be explored further in the subsequent sections.

RMS values of the single residual curves range in 7.1 and 14.9 W m^{-2} . Permutations using PIOMAS sea ice data, which exhibit a smoother annual cycle of $\{\text{MET}\}$ (Fig. 3d), tend to attain smaller residual values. Consequently, the optimal combination (i.e., the combination yielding the smallest RMS value) is CERES-EBAF and ERA5 for the atmospheric terms, C-GLORSv7 for $\{\text{OHCT}\}$, PIOMAS for $\{\text{MET}\}$, and ARCGATE for $\{\nabla \cdot F_O\}$. The annual cycle of the budget residual for this “best” combination is shown in red in Fig. 6. Removal of the yearly mean bias reduces the RMS values to the range 6.4 – 14.8 W m^{-2} .

Budget residuals $\{R\}$ computed from the estimates by SB14 are shown in Fig. 6 as well. The SB14 values are derived from their Table 3.2 using our definition of $\{R\}$. The resulting curve looks fairly different compared to our residuals, with maximum values of -8 W m^{-2} in summer and minimum values of -47 W m^{-2} in winter. Full (bias-corrected) RMS values are 34.6 (14.9) W m^{-2} . The large difference between the latter two values indicates a large bias in their results. Our ensemble-mean full (bias-corrected) RMS value thus is reduced by $\sim 72\%$ ($\sim 42\%$) compared to SB14 and hence demonstrates a major improvement in both yearly mean bias and shape of the annual cycle.

We note that the comparison to SB14 in Fig. 6 contains an inconsistency in the sense that SB14 did not account for the “secondary terms” $\{\text{IHCT}\}$ and $\{\text{MET}_{\text{snow}}\}$. If we neglect these terms also in our residual estimates, the RMS values of $\{R\}$ reduces to a range of 5.5 to 12.8 W m^{-2} or even 4.1 to 12.6 W m^{-2} when bias-corrected, as the minima and maxima in June and October become less pronounced (not shown). This is because these secondary terms show similar seasonal variations as the main storage terms (cf. Figs. 3c and 3d). Hence, the RMS reduction compared to SB14 would be even more substantial than stated above. However, this result also gives further rise to the presumption that the storage terms require too much energy in May–June and release too much energy in October–November (i.e., they exhibit a too strong annual cycle). The prime candidate for this overestimation is MET, which is only weakly constrained by observations and will be assessed in the subsequent section.

3) VALIDATION OF THE SEA ICE ANNUAL CYCLE IN ORAS5

Results in the previous sections suggest an overly strong seasonal cycle in the ocean storage terms. Here

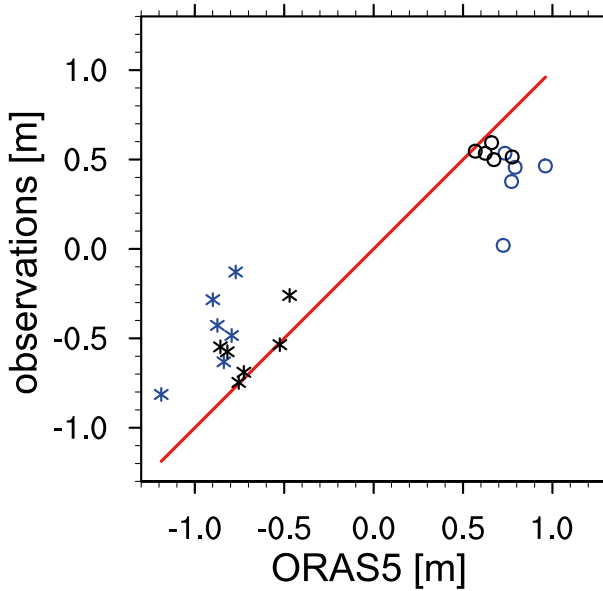


FIG. 7. Scatterplot of study area average thickness differences (in m) between subsequent fall and winter missions (blue circles) and vice versa (blue stars) for *ICESat*/ORAS5 and differences between November and March monthly averages (black circles) and vice versa (black stars) for CS2SMOS/ORAS5. The red line represents the 1:1 line.

we compare the seasonal cycle of reanalyzed sea ice with satellite estimates to further investigate the strength of the {MET} annual cycle. Several earlier studies have investigated sea ice thickness in observations and reanalyses (e.g., Balan Sarojini et al. 2019; Uotila et al. 2019), but here we are interested in seasonal changes of sea ice thickness, since this is the relevant quantity for the annual cycle of the energy budget.

Figure 7 shows changes in mean sea ice thickness over the Arctic Ocean from fall to winter and from winter to fall for *ICESat*/ORAS5, and from November to March and March to November for CS2SMOS/ORAS5. All growth values lie right of the 1:1 line, and all melt values lie left of the 1:1 line. Regression coefficients of thickness changes are 1.7 m m^{-1} for *ICESat* versus ORAS5 and 1.2 m m^{-1} for CS2SMOS versus ORAS5, indicating that the seasonal cycle of Arctic sea ice thickness in ORAS5 is 70% higher than in *ICESat* observations and 20% higher than in CS2SMOS observations. We note that there is some doubt about the realism of the *ICESat* seasonal cycle. For instance, the 2003/04 winter growth from *ICESat* of 0.02 m (see Fig. 7) seems implausibly small. Other reanalyses exhibit a similar or even more pronounced seasonal cycle when compared to CS2SMOS (not shown).

We now take a closer look at the spatial distribution of the sea ice thickness discrepancies between ORAS5 and observations. Figure 8 presents maps of the difference in winter sea ice growth between ORAS5 and CS2SMOS (Fig. 8a) and ORAS5 and *ICESat* (Fig. 8b). Both spatial patterns are quite similar. Hence, when compared to observations, ORAS5 sea ice growth is too weak in thick ice regions and too strong in thin ice regions. The overly strong ice thickness growth in thin-ice regions is present also in the other reanalysis products used here (not shown).

Another way of demonstrating the overly strong annual cycle of MET is to look at the melt season, for which there are no satellite-based sea ice thickness observations available. The alternative approach we choose here is to compare sea ice melt to net surface

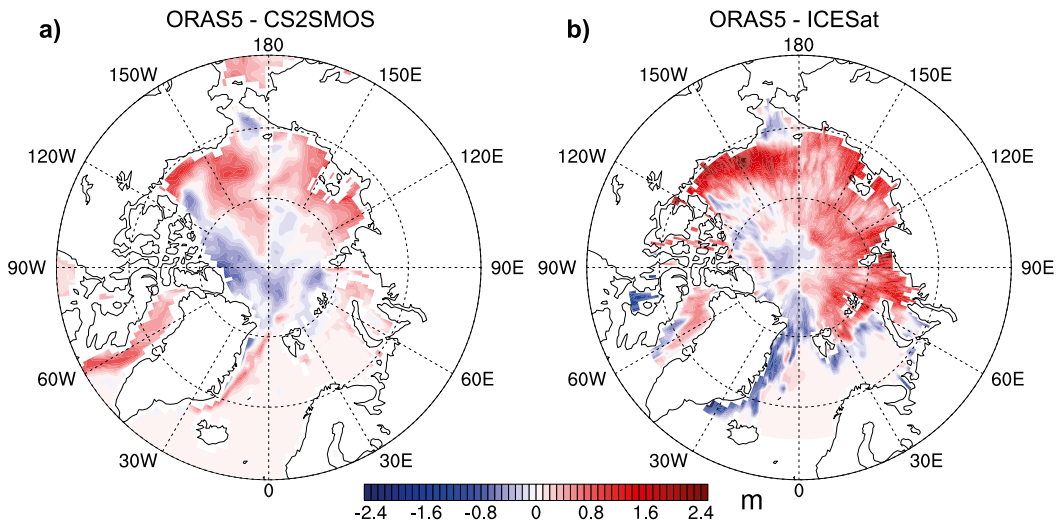


FIG. 8. Difference in thickness change from (a) November to March between ORAS5 and CS2SMOS and (b) from September/October to February/March between ORAS5 and *ICESat*.

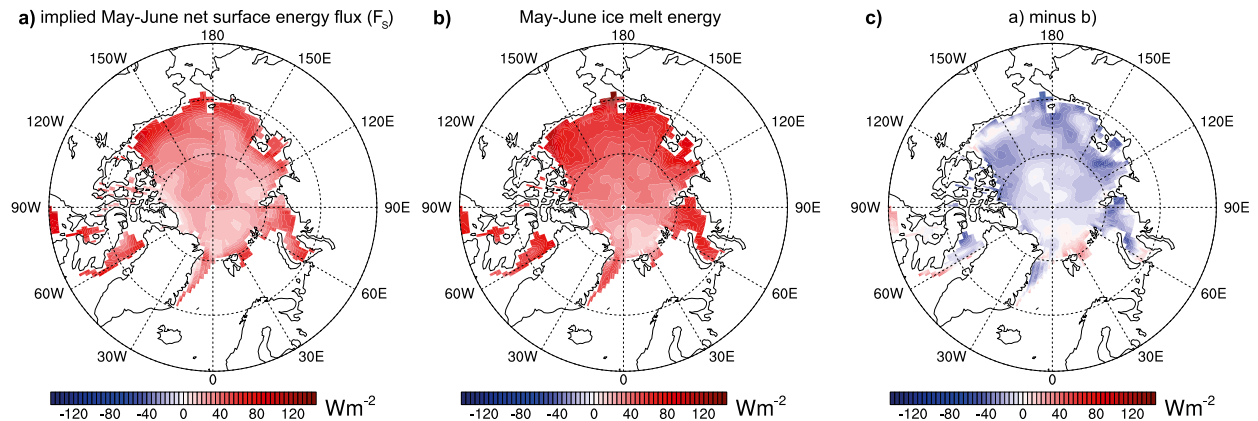


FIG. 9. May–June mean (a) inferred F_S estimated from CERES-EBAF net TOA fluxes and ERA5 atmospheric transports and (b) energy required from sea ice melt (shown is the average of ORAS5, PIOMAS, CGLORSv7, and CGLORSv5) in areas where sea ice concentration is $>30\%$. (c) The difference of (a) and (b).

energy input, which during early summer is responsible for most of the sea ice melt, both via direct vertical fluxes into the sea ice and via ocean–sea ice energy fluxes fed by atmospheric energy input (Steele et al. 2010). Inspection of ORAS5 data confirmed that lateral ocean heat convergence is indeed small in the areas of strong seasonal ice reduction (not shown).

Figure 9 shows May–June averages of (i) net surface energy flux (F_S) inferred using ERA-Interim and CERES-EBAF data, (ii) energy required for sea ice melt (MET) derived from the ORAS5 sea ice state, and (iii) their difference in regions with sea ice concentration $>30\%$. It is evident that MET is substantially higher than F_S , with differences as large as $20\text{--}30\text{ W m}^{-2}$ over large regions. The F_S deficit is largest toward the Siberian and Canadian coast, which are exactly the regions where sea ice growth during fall/winter has been found to be too strong when compared to satellite-based sea ice thickness data (cf. Fig. 8; note the opposite sign due to the negative definition of L_f). These results thus further confirm the finding that the annual cycle of MET is too strong in the reanalysis-based sea ice data used here. Inspection of ORAS5 data reveals that especially in the Beaufort Sea the overly strong sea ice melt (i.e., too high MET) is related to negative sea ice concentration increments (not shown). Negative sea ice concentration increments in ORAS5 imply negative sea ice volume increments, as these are proportional to the sea ice concentration increments with the model sea ice thickness as a proportionality factor. Since sea ice in ORAS5 is very thick in the Beaufort Sea at the beginning of the melt season, negative sea ice concentration increments lead to overly strong negative volume increments in this region (Tietsche et al. 2013, 2014).

An overall conclusion from this and the previous section is that the MET annual cycle is too strong in the reanalyses. This is supported by three independent lines of evidence: the annual cycle of the budget residual shown in Fig. 6, direct comparison to satellite-based sea ice data in winter, and comparison to surface energy fluxes in spring (this section). Therefore, there is high confidence in the verdict that the reanalyses have too much sea ice growth in winter and too much sea ice melt in summer.

5. Synthesis and discussion

In this section we present our best estimate of the Arctic energy budget 2005–09. The best estimate is obtained through the variational adjustment procedure outlined in section 2, using the quantifications of the physical terms and their uncertainties in the earlier sections. The practical implementation is as follows. As a priori estimates we use the data combination that yields the smallest budget residual based on results in Fig. 6, namely the combination of CERES-EBAF, ERA5, C-GLORSv7, PIOMAS, and ARCGATE. Uncertainties are estimated using results discussed in section 4. Specifically, we use the spread shown in Fig. 4 to derive σ'_i . The number of individual estimates for the different terms is small, and hence we conservatively assume that the maximum spread of every curve in Fig. 4 is a rough estimate of $\pm 1\sigma_i$. In this way we obtain the following uncertainty estimates: $\sigma'_{\{V_{FA}\}} = 3.9\text{ W m}^{-2}$, $\sigma'_{\{AET\}} = 0.5\text{ W m}^{-2}$, $\sigma'_{\{MET\}} = 12.7\text{ W m}^{-2}$, $\sigma'_{\{OHCT\}} = 5.7\text{ W m}^{-2}$, $\sigma'_{\{V_{FO}\}} = 3.7\text{ W m}^{-2}$, and $\sigma'_{\{V_{FI}\}} = 0.8\text{ W m}^{-2}$. One-sigma uncertainty of $\{MET_{\text{snow}}\} + \{IHCT\}$ is assumed 2 W m^{-2} . The one-sigma uncertainty of $\{Rad_{TOA}\}$ is estimated to be 0.5 W m^{-2} , based on the standard

TABLE 3. 2005–09 *adjusted* mean annual cycle of the coupled Arctic energy budget; units are W m^{-2} (conversion factor to obtain TW is 10.51). {IHCT} and {MET_{snow}} are combined to secondary (2ry) terms.

	{Rad _{TOA} }	$-\{\nabla \cdot F_A\}$	{AET}	{F _S } _{implied}	{MET}	{OHCT}	$-\{\nabla \cdot F_O\}$	$-\{\nabla \cdot F_I\}$	{2ry}
Jan	-176.9	123.3	5.9	-59.5	-22.0	-14.3	19.3	2.3	-1.6
Feb	-175.5	112.8	-2.8	-59.9	-24.8	-17.0	14.2	2.1	-1.9
Mar	-149.8	110.3	11.3	-50.8	-21.8	-11.2	14.2	2.8	-0.9
Apr	-99.0	102.1	25.7	-22.6	-11.9	-0.6	10.0	2.3	2.1
May	-45.9	82.3	21.6	14.8	5.2	14.5	10.7	1.3	7.1
Jun	8.7	84.7	22.5	70.9	45.9	31.6	11.5	0.5	5.4
Jul	12.4	87.9	5.8	94.4	61.3	47.2	13.9	0.2	0.0
Aug	-64.5	86.9	-22.3	44.7	26.5	33.5	14.8	0.1	-0.3
Sep	-148.6	98.1	-27.3	-23.2	3.7	-6.1	18.8	0.6	-1.4
Oct	-185.0	96.5	-19.6	-68.9	-10.2	-35.4	19.1	1.5	-2.7
Nov	-186.0	106.6	-8.0	-71.4	-23.7	-22.2	21.1	1.8	-2.6
Dec	-179.5	103.4	-13.5	-62.7	-23.8	-16.5	18.1	1.5	-2.7
Mean	-115.8	99.6	-0.1	-16.2	0.4	0.3	15.5	1.4	0.0

deviation of the monthly Arctic mean TOA net flux from *Terra* and *Aqua* satellites. In practice, we perform the adjustment in two steps. First, only the flux terms are adjusted in a way to match the long-term storage rates (i.e., to yield long-term mean closure). In a second step, the monthly climatologies of all terms are adjusted to close the budget on a monthly scale. We use the same uncertainty estimates for both steps of the adjustment.

The results after the variational adjustment procedure are presented in Table 3. *Unadjusted* results are given in appendix B (Table B1). Comparison of adjusted and unadjusted results reveals that none of the adjustments was larger than one standard deviation of the error, and hence they are considered reasonably small. Since the general features of the annual cycles have been discussed already in section 4a, we limit the discussion here to a comparison to Table 3.2 in SB14 and remaining uncertainties. For reference, appendix A (Table A3) shows variationally adjusted climatologies for the polar cap (70°–90°N), using the same uncertainty estimates as for the Arctic Ocean domain.

Our results for net radiation at TOA and atmospheric energy storage agree very well with those of SB14. This is because SB14 used satellite-based TOA radiation as well, and uncertainties in atmospheric state quantities are deemed small. Comparing to SB14, the agreement for atmospheric energy divergence is good between June and October when transports are more moderate ranging between 82 and 96 W m^{-2} . However, our results indicate much stronger transports in winter with values up to 123 W m^{-2} in January. Results in SB14 do not show this winter strengthening, resulting also in a considerably lower yearly mean of $-\{\nabla \cdot F_A\}$ (84 W m^{-2} compared to our estimate of $\sim 100 \text{W m}^{-2}$). The reason for the rather strong discrepancy to SB14 in winter is unclear; most likely it is related to problems in the ERA-40

reanalysis used by SB14. Tests showed that effects of spectral truncation on our results are small, but differences in land–sea masks and SB14’s neglect of Baffin Bay might play an additional role.

The melt energy tendency {MET} exhibits the largest adjustments in our variational procedure (up to 10 W m^{-2} in October) among all the energy budget terms. This is a consequence of its relatively large spread. The amplitude of the annual cycle of {MET} is thereby slightly reduced, but still seems large when compared with satellite-based CS2SMOS data. Our {MET} average for November–March is -23.2W m^{-2} , while the CS2SMOS-based November–March average is only -15.3W m^{-2} . The SB14 estimate for November–March is even more negative than ours (-25.8W m^{-2}). We computed the {MET} annual cycle also for the CS2SMOS period, and the results were very similar. Thus, differences in the periods considered can be ruled out as cause for the discrepancy. One possible reason for our reanalysis-based {MET} estimate being too high is the fact that reanalyses use a minimum sea ice thickness on the order of $\sim 0.5 \text{m}$ (Tietsche et al. 2018); that is, energetic effects of initial freeze up are likely overestimated. On the other hand, data from the SMOS satellite used in the CS2SMOS product might underestimate sea ice growth once a thickness of $\sim 1 \text{m}$ is reached.

The amplitude of the seasonal cycles of ocean heat content tendency {OHCT} and {MET} are similar (RMS values of the annual cycles are 28.2 and 27.5 W m^{-2} , respectively), unlike the results of SB14, who found a considerably higher seasonal amplitude for {MET} than for {OHCT}. There are, however, qualitative differences when compared to SB14. Our results indicate that seasonal ocean warming peaks in July rather than June, which is more consistent with the maximum of {Rad_{TOA}}

and smaller sea ice extent with consequently higher absorption compared to June. The largest discrepancy with SB14 occurs in October (31.2 W m^{-2}), when our results indicate already strong ocean cooling. Given the lack of sufficient in situ ocean observation, it is difficult to judge which result is more realistic. We note that all our residual curves exhibit a peak in October, indicating data inconsistencies during this calendar month (see Fig. 6). The large {OHCT} spread in depths below 300 m (see Fig. 2a) is unlikely to affect the uncertainties of the {OHCT} seasonal cycle too much, because the annual cycle is small at these depths.

Adjustments to oceanic heat transport are small ($<1 \text{ W m}^{-2}$ in every calendar month), which easily is within uncertainty bounds provided by Tsubouchi et al. (2018). Our estimate of $\{-\nabla \cdot F_O\}$ of 15.5 W m^{-2} is thus very close to observations and deemed credible. In the light of our results, the model-based estimate given by SB14 (3 W m^{-2}) appears far too low. A possible cause of this underestimation is that the ocean circulation at high latitudes as simulated by their low-resolution ocean model was simply too weak, and hence was unable to reproduce the observed heat transports in the high latitudes.

Last, we turn to the net air–sea energy exchange $\{F_S\}$. Our best estimate of yearly mean $\{F_S\}$ over the Arctic Ocean is -16.2 W m^{-2} , which exactly balances our estimates for ocean heat accumulation (0.7 W m^{-2}) and lateral oceanic transports (16.9 W m^{-2}) during the 2005–09 period. We believe this value is robust for the following reasons. On yearly scales, the large spread in the annual cycle of oceanic storage terms does not play a role and hence does not affect the uncertainty of the annual means. The ARCGATE ocean heat transport estimate is based on observations over rather narrow oceanic sections, which leaves little room for large inaccuracies. The agreement of the a priori estimates is already very good and only small yearly mean adjustments were needed, with the largest adjustment for $\{\nabla \cdot F_A\}$ (0.9 W m^{-2}) and $\{\nabla \cdot F_O\}$ (0.7 W m^{-2}) (cf. Tables 2 and B1). The annual cycle of $\{F_S\}$ is constrained by data from both sides of the interface (atmosphere and ocean/sea ice) rather than only one as is common in other assessments. As a consequence, $\{F_S\}$ estimates given in SB14 based on parameterized reanalysis fluxes (-11 W m^{-2}) are likely too weak and those inferred from their atmospheric budget terms (-31 W m^{-2}) are probably too strong.

The 5-yr period covered by the present study is likely too short to filter out natural variability, but this is dictated by the current availability of mooring-derived oceanic fluxes. While the estimates of annual mean fluxes are robust (cf. 2005–09 and 2001–17 averages in

Table 2), tests showed that monthly climatologies of the different terms can easily differ by $\sim 5 \text{ W m}^{-2}$ when considering different 5-yr periods. Another aspect is seasonal trends in the Arctic energy budget, as documented by Hartmann and Ceppi (2014) and Mayer et al. (2016). Hence, the results presented here are a best estimate for 2005–09, including the imprint of natural and forced variability present at that time, and likely would not be identical for a different 5-yr period.

6. Summary and conclusions

Our estimates of long-term (2001–17) heat accumulation in the Arctic indicate that the regional energy imbalance of the Arctic Ocean domain is in the order of 1 W m^{-2} , with 2/3 going into the warming of the ocean water and 1/3 going into sea ice, respectively. This is in agreement with earlier results (von Schuckmann et al. 2018; Mayer et al. 2016). It also confirms observation- (Mayer et al. 2016) and model-based (Burgard and Notz 2017) results indicating that the current regional energy imbalance in the Arctic Ocean is similar to global average values. Values for the ocean north of 70°N indicate higher ocean warming rates in the range of 1.1 to 1.6 W m^{-2} . This seems to be related to atmospheric and oceanic decadal variability in the area north of 70°N but south of the boundaries of our Arctic Ocean domain (see Robson et al. 2012), rather than a sign of Arctic amplification in the ocean energy budget. Comparison of different estimates of ocean warming suggests that agreement in the upper 300 m is good, but uncertainties are large below, especially in the 300–700-m layer, where more in situ profiles are needed.

The closure of our estimates is very good on an annual-mean basis already without imposing a closed energy budget. This is remarkable, given that the individual terms are derived from largely independent observational and reanalysis products. Total energy convergence is too weak by ~ 1 to 8 W m^{-2} , depending on the choice of data products. The smallest 2005–09 long-term mean residual of 1 W m^{-2} is found for the combination of CERES-EBAF TOA fluxes, ERA5 atmospheric energy transports and storage, and ocean heat transport from the mooring-derived ARCGATE dataset. Ocean heat transports from ocean reanalyses seem to be too weak by 10%–20% compared to those from ARCGATE.

Our results represent a major improvement over the earlier estimates by SB14. Their fluxes into the Arctic Ocean domain indicate an imbalance in the order of 20 W m^{-2} , mainly because their estimates of both atmospheric and oceanic heat transports were too low. We note that even for climate models, exact closure is not necessarily granted (Hobbs et al. 2016), and thus an

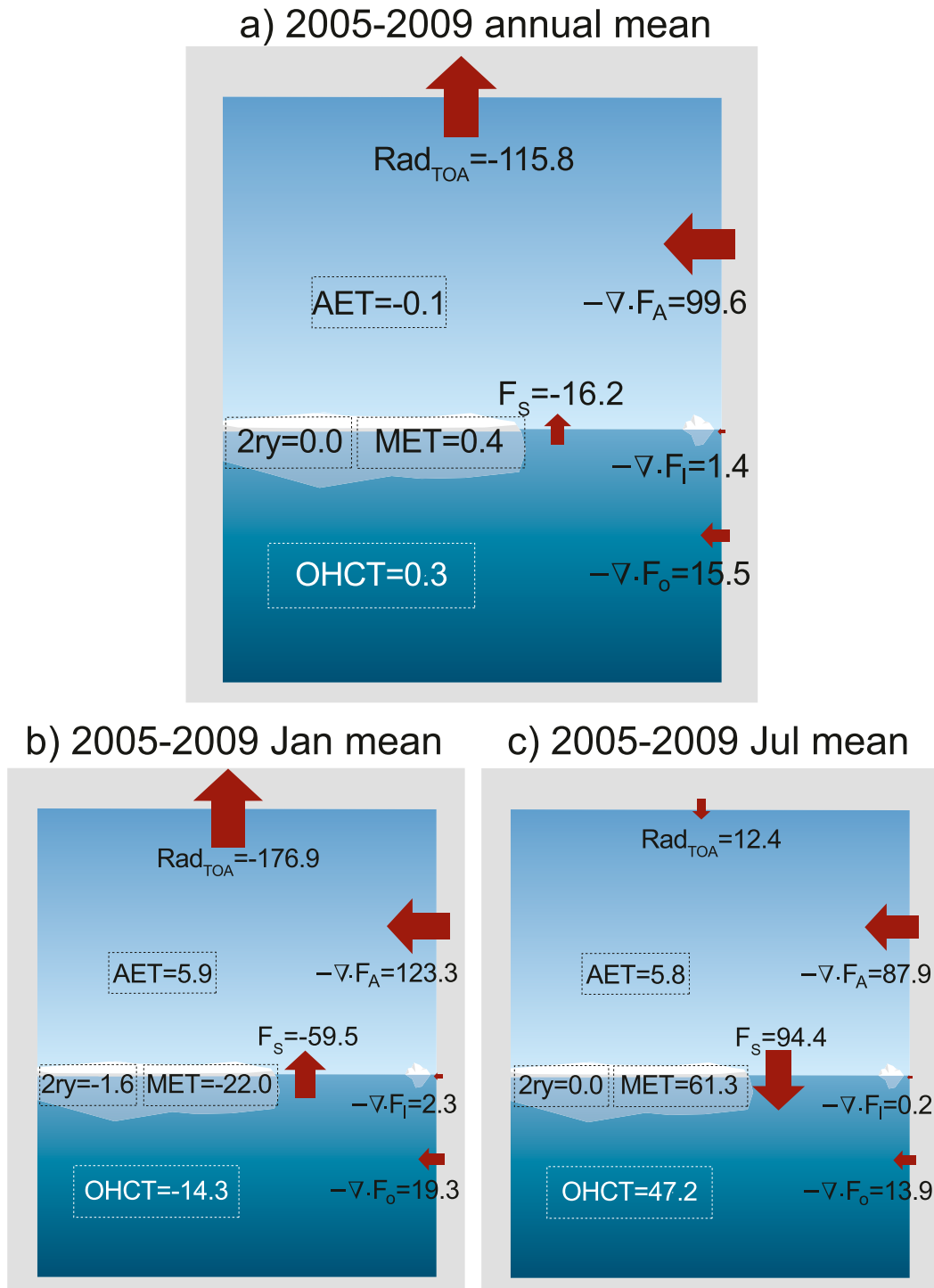


FIG. 10. Energy storage and flux terms (in $W m^{-2}$) for the Arctic Ocean domain. Shown are the (a) annual, (b) January, and (c) July mean based on the variationally adjusted 2005–09 data shown in Table 3. The arrows are scaled by the square root of their magnitude. Note that here MET is based on PIOMAS and OHCT is based on CGLORSv7, as described in the text. See Table 1 for other estimates of long-term heat storage. The graphic design of the schematic is adapted from Pietschnig (2016).

imbalance on the order of 1 W m^{-2} should be deemed a very small value.

For the polar cap (ocean and land north of 70°N), the long-term closure is slightly worse. Total energy convergence is too weak by $8\text{--}10 \text{ W m}^{-2}$. Reasons are the lack of in situ-based ocean transports for this region, which are likely underestimated by ocean reanalyses (see above) and possibly also too weak poleward atmospheric energy transports in the reanalyses (as suggested by too low values of inferred F_S over land).

Quantification of the mean annual cycle of the coupled Arctic energy budget confirms the well-known picture that the large annual cycle in net radiative energy input is mainly balanced by ocean storage terms (OHCT and MET) and to a lesser degree by atmospheric energy storage and atmospheric lateral energy convergence. The seasonal cycle in ocean heat transports is comparatively weak. Small but nonnegligible contributions to the energy budget stem from sea ice sensible heat and snow. Uncertainties in the mean annual cycle are larger compared to the annual mean estimates, and there are sizeable budget residuals when comparing the monthly climatologies of the budget terms. Several lines of evidence (budget arguments and direct comparison to satellite-based estimates) suggest that the annual cycle in sea ice volume in the reanalysis data used here is overestimated, confirming results from earlier studies (Tietsche et al. 2014; Uotila et al. 2019). However, optimal data combination yields a full (bias-corrected) RMS value of the residual of only 7.1 (6.4) W m^{-2} . When considering the ensemble mean residual of our input data, the full (bias-corrected) RMS value is 9.9 (9.5) W m^{-2} , which represents a substantial reduction of the residual RMS value by $\sim 72\%$ ($\sim 36\%$) compared to SB14.

We subsequently applied a variational adjustment procedure to obtain budget closure for every calendar month, requiring only moderate adjustments to the single terms. These results can serve as reference estimates for both the observational and modeling communities. Annual mean fluxes and storage as well as the means for January and July are depicted in Fig. 10, which presents a much more consistent and accurate picture of the Arctic energy budget than earlier work.

In conclusion, our results and their improvements over earlier assessments demonstrate the recent progress made in observational capabilities, data assimilation techniques, and diagnostic methods. To reduce uncertainties further, a larger number of deep ocean observations in the Arctic Ocean are needed to better constrain ocean reanalyses. The major problem is the sheer lack of observations, which seems to become gradually ameliorated (e.g., Toole et al. 2011; Riser et al. 2016). Another issue appears to be the oftentimes fragmentary ingestion of available information (e.g., Behrendt et al. 2018) into global profile databases that typically are used at data assimilation centers (e.g., EN4). The largest uncertainties in our assessment of the Arctic seasonal cycle stem from sea ice thickness, which is no surprise given the fact that currently operational reanalyses assimilate only sea ice concentration. Reliable sea ice thickness observations and their robust assimilation into reanalyses are needed to further reduce uncertainties in future estimates of the Arctic energy budget. New observational products like ICESat-2 and ongoing research at data assimilation centers represent activities toward this goal. Finally, we note evident importance of longer mooring-derived ocean heat transport time series. Currently, the ARCGATE dataset covers only 2005–09, but there is potential for extension of the time series up to present, as all four main Arctic gateways have been monitored continuously since summer 2004 (Dickson et al. 2008). Such an extension would offer a unique opportunity for long-term monitoring of the coupled Arctic energy budget.

Acknowledgments. The authors thank Ron Kwok for helpful discussion on ICESat data, Robert Ricker for clarifications concerning CS2SMOS data, Norman Loeb for comments on our uncertainty estimates of CERES-EBAF fluxes, and Simon Witter for help with Fig. 10. This work has been funded through the European Union's Horizon 2020 research and innovation programme under Grant Agreements 633211 (AtlantOS) and 640161 (SPICES), as well as from the Austrian Science Fund project P28818. TT's involvement was partially supported by the EU's Horizon 2020 Marie Skłodowska-Curie Grant Agreement 652757.

TABLE A1. 2005–09 (2001–17 values shown in parentheses) rates of change in the three main storage terms averaged over the polar cap ($70^\circ\text{--}90^\circ\text{N}$); units are W m^{-2} with regard to the ocean plus land area north of 70°N . The asterisk denotes 2001–15 values.

	[OHCT]	[MET]	[OHCT] + [MET]	[AET]
ORAS5	0.71 (0.9)	0.32 (0.17)	0.98 (1.07)	—
C-GLORS v7	0.56 (0.61)	0.24 (0.22)	0.80 (0.82)	—
C-GLORS v5	0.78 (0.86*)	0.23 (0.29*)	0.94 (1.12*)	—
PIOMAS	—	0.27 (0.25)	—	—
ERA-Interim	—	—	—	-0.01 (0.01)

TABLE A2. 2005–09 (2001–17 values shown in parentheses) mean energy fluxes into the polar cap; units are W m^{-2} with regard to the ocean plus land area north of 70°N . The asterisk denotes 2001–15 values. SB14 values are based on various periods, mainly before the 2000s (see their Table 3.1).

	[Rad _{TOA}]	$-\nabla \cdot F_A$	$[F_S]_{\text{implied}}$	$-\nabla \cdot F_O$	$-\nabla \cdot F_I$
CERES-EBAF 4.0	−114.6 (−115.0)				
ERA-Interim		94.8 (94.8)	−19.8 (−20.2)		
JRA-55		93.3 (93.6)	−21.3 (−21.5)		
ERA5		95.5 (95.6)	−19.1 (−19.4)		
ORASS			—	13.6 (13.1)	—
C-GLORS v7			−13.5 (−12.2)	13.8 (13.0)	0.1 (0.0)
C-GLORS v5			−12.4 (−11.5*)	13.0 (12.4*)	0.3 (0.2*)
SB14	−110	100	−10	—	—

APPENDIX A

Polar Cap (70°–90°N) Results

Tables A1 and A2 provide 2005–09 (2001–17) long-term averages of the main budget terms, similar to Tables 1 and 2 in the main text, but averaged over the polar cap north of 70°N (indicated by the square brackets). Values are with respect to the total ocean plus land area north of 70°N . The conversion factor to obtain ocean-area averages [as provided, e.g., in Mayer et al. (2016)] is 1.38 and the conversion factor to obtain TW is 14.78.

For consideration of the mean annual cycle of the polar cap energy budget (displayed in Table A3), it is necessary to include land. The atmosphere–land energy budget equation over land reads as follows:

$$\text{Rad}_{\text{TOA}} - \text{AET} - \nabla \cdot F_A = \text{MET}_{\text{snow}} + \text{LHCT} + R. \quad (\text{A1})$$

Compared to the total column budget over ocean [Eq. (4) in the main text], there appears a land heat storage term LHCT (land heat content tendency) in Eq. (A1). The annual cycle of LHCT is sizeable. However, since the land energy budget is not the focus of this paper, we estimate

the sum $\text{MET}_{\text{snow}} + \text{LHCT}$ from the net surface energy flux as output from the employed atmospheric reanalyses. For the polar cap mean annual cycle we compute an appropriately weighted average (according to the partition of the total area into land and ocean area) of the terms in Eq. (A1) and Eq. (4).

APPENDIX B

Unadjusted Mean Annual Cycle of the Arctic Ocean Energy Budget

Values in Table B1 are the same as in Table 3 in the main text, but without the variational adjustment to enforce a closed energy budget.

APPENDIX C

List of Acronyms

AE(T)	Atmospheric total energy (tendency)
ARCGATE	Mooring-derived data of oceanic fluxes through the Arctic gateways

TABLE A3. 2005–09 *adjusted* mean annual cycle of the coupled polar cap ($70^\circ\text{--}90^\circ\text{N}$) energy budget; units are W m^{-2} (conversion factor to obtain TW is 14.78). [LHCT] and [MET_{snow}] are combined to secondary terms (2ry).

	[Rad _{TOA}]	$-\nabla \cdot F_A$	[AET]	$[F_S]_{\text{implied}}$	[MET]	[OHCT]	$-\nabla \cdot F_O$	$-\nabla \cdot F_I$	[2ry]
Jan	−174.1	122.8	6.3	−57.6	−16.3	−12.3	20.5	1.5	−6.9
Feb	−173.6	112.3	−2.4	−58.9	−18.2	−17.1	15.9	0.4	−7.2
Mar	−147.3	106.8	10.2	−50.7	−17.8	−12.3	15.4	0.5	−4.7
Apr	−97.5	102.7	26.2	−21.0	−9.3	2.3	14.7	0.7	1.5
May	−45.1	81.0	20.1	15.7	2.3	15.4	12.0	−1.0	9.0
Jun	8.8	78.4	21.0	66.2	34.8	24.7	10.2	−1.0	15.9
Jul	10.3	80.1	5.6	84.6	48.0	37.2	13.6	0.2	13.5
Aug	−66.0	85.0	−21.1	40.1	24.3	25.2	15.7	0.2	6.4
Sep	−146.9	96.5	−27.2	−23.2	3.4	−4.0	19.1	0.2	−3.4
Oct	−183.0	100.8	−19.2	−63.0	−11.4	−23.6	18.8	0.2	−9.1
Nov	−183.2	110.2	−8.6	−64.4	−19.5	−17.1	18.3	0.5	−9.0
Dec	−176.8	108.5	−11.0	−57.3	−17.5	−11.5	18.9	1.1	−8.3
Mean	−114.5	98.8	0.0	−15.8	0.2	0.6	16.1	0.3	−0.2

TABLE B1. 2005–09 *unadjusted* mean annual cycle of the coupled Arctic Ocean energy budget; units are W m^{-2} (conversion factor to obtain TW is 10.51). IHCT and MET_{snow} are combined to secondary terms.

	{Rad _{TOA} }	$-\{\nabla \cdot F_A\}$	{AET}	$\{F_S\}_{\text{impl}}$	{MET}	{OHCT}	$-\{\nabla \cdot F_O\}$	$-\{\nabla \cdot F_I\}$	{2ry}	{R}
Jan	-176.9	122.5	5.9	-60.2	-23.0	-14.5	18.7	2.3	-1.6	-0.1
Feb	-175.5	111.6	-2.8	-61.1	-21.6	-16.3	13.3	2.0	-1.8	-6.0
Mar	-149.8	108.9	11.3	-52.2	-16.6	-10.2	13.1	2.7	-0.8	-8.9
Apr	-99.0	100.8	25.7	-23.9	-7.6	0.3	8.9	2.2	2.2	-7.6
May	-45.9	80.9	21.6	13.4	10.8	15.6	9.5	1.2	7.2	-9.5
Jun	8.7	83.4	22.5	69.6	50.3	32.5	10.4	0.5	5.5	-7.8
Jul	12.4	87.1	5.8	93.7	60.0	47.0	13.3	0.2	0.0	0.2
Aug	-64.5	85.9	-22.3	43.7	27.8	33.8	14.1	0.1	-0.3	-3.4
Sep	-148.6	97.3	-27.3	-24.0	3.4	-6.2	18.2	0.5	-1.4	-1.1
Oct	-185.0	96.7	-19.7	-68.7	-20.5	-37.4	19.3	1.5	-3.0	13.0
Nov	-186.0	106.5	-8.0	-71.5	-31.2	-23.7	21.1	1.8	-2.8	9.1
Dec	-179.5	102.8	-13.5	-63.2	-27.2	-17.2	17.7	1.5	-2.8	3.2
Mean	-115.8	98.7	-0.1	-17.0	0.4	0.3	14.8	1.4	0.0	-1.6

c	Ocean current vector	L_f	Latent heat of fusion
c_a	Specific heat of dry air at constant pressure	LHCT	Land heat content tendency
CERES-EBAF	Clouds and the Earth's Radiant Energy System–Energy Balanced and Filled	L_v	Latent heat of vaporization
C-GLORS	CMCC Global Ocean Reanalysis System	ME(T)	Latent heat (tendency) associated with changing ice mass
c_i	Sea ice drift vector	MET_{snow}	Latent heat tendency associated with changing snow mass
c_i	Specific heat of sea ice	M_{snow}	Energy going into snowmelt
CMCC	Centro Euro-Mediterraneo sui Cambiamenti Climatici	OHCT(T)	Ocean heat content (tendency)
c_p	Specific heat of seawater	ORAS5	ECMWF's Ocean Reanalysis System 5
CS2SMOS	Sea ice product merged from <i>Cryosat-2</i> and Soil Moisture and Ocean Salinity satellites	p	Atmospheric pressure
d_i	Gridpoint average sea ice thickness	ϕ	Geopotential
d_{snow}	Gridpoint average snow depth	PIOMAS	Pan-Arctic Ice Ocean Modeling and Assimilation System
ECMWF	European Centre for Medium-Range Weather Forecasts	P_{snow}	Snowfall rate
ERA5	ECMWF's fifth atmospheric reanalysis	q_g	Atmospheric water vapor content
ERA-40	40-yr ECMWF Re-Analysis	Rad_{TOA}	Net radiation at the top of the atmosphere (TOA)
ERA-Interim	ECMWF interim reanalysis	ρ_0	Sea water density
f	Sea ice fraction	ρ_i	Sea ice density
F_A	Vertically integrated atmospheric energy transport	ρ_{snow}	Snow density
F_b	Net energy flux at ice–ocean interface	T_{00}	Reference temperature (-1.8°C)
F_I	Latent heat transport associated with sea ice	T_a	Air temperature
F_O	Vertically integrated ocean heat transport	T_p	Precipitation temperature
F_S	Net surface energy flux	v	Horizontal wind vector
g	Gravitational acceleration		
ICESat	<i>Ice, Cloud, and Land Elevation Satellite</i>		
IHCT	Sea ice sensible heat content tendency		
JMA	Japan Meteorological Agency		
JRA-55	Japanese 55-year Reanalysis		
k	Kinetic energy		

REFERENCES

- Allard, R. A., and Coauthors, 2018: Utilizing CryoSat-2 sea ice thickness to initialize a coupled ice–ocean modeling system. *Adv. Space Res.*, **62**, 1265–1280, <https://doi.org/10.1016/j.asr.2017.12.030>.
- Balan Sarojini, B., S. Tietsche, M. Mayer, M. Balmaseda, and H. Zuo, 2019: Towards improved sea ice initialization and forecasting with the IFS. ECMWF Tech. Memo. 844, 30 pp., <https://www.ecmwf.int/sites/default/files/elibrary/2019/18918-towards-improved-sea-ice-initialization-and-forecasting-ifs.pdf>.

- Balmaseda, M. A., K. Mogensen, and A. T. Weaver, 2013: Evaluation of the ECMWF ocean reanalysis system ORAS4. *Quart. J. Roy. Meteor. Soc.*, **139**, 1132–1161, <https://doi.org/10.1002/qj.2063>.
- , and Coauthors, 2015: The Ocean Reanalyses Intercomparison Project (ORA-IP). *J. Oper. Oceanogr.*, **8**, s80–s97.
- Behrendt, A., H. Sumata, B. Rabe, and U. Schauer, 2018: UDASH—Unified Database for Arctic and Subarctic Hydrography. *Earth Syst. Sci. Data*, **10**, 1119–1138, <https://doi.org/10.5194/essd-10-1119-2018>.
- Bourassa, M. A., and Coauthors, 2013: High-latitude ocean and sea ice surface fluxes: Challenges for climate research. *Bull. Amer. Meteor. Soc.*, **94**, 403–423, <https://doi.org/10.1175/BAMS-D-11-00244.1>.
- Brakstad, A., K. Våge, L. Håvik, and G. W. K. Moore, 2019: Water mass transformation in the Greenland Sea during the period 1986–2016. *J. Phys. Oceanogr.*, **49**, 121–140, <https://doi.org/10.1175/JPO-D-17-0273.1>.
- Burgard, C., and D. Notz, 2017: Drivers of Arctic Ocean warming in CMIP5 models. *Geophys. Res. Lett.*, **44**, 4263–4271, <https://doi.org/10.1002/2016GL072342>.
- Cullather, R. I., and M. G. Bosilovich, 2012: The energy budget of the polar atmosphere in MERRA. *J. Climate*, **25**, 5–24, <https://doi.org/10.1175/2011JCLI4138.1>.
- Dee, D. P., and Coauthors, 2011: The ERA-Interim reanalysis: Configuration and performance of the data assimilation system. *Quart. J. Roy. Meteor. Soc.*, **137**, 553–597, <https://doi.org/10.1002/qj.828>.
- Dickson, B., J. Meincke, and P. Rhines, 2008: Arctic–subarctic ocean fluxes: Defining the role of the northern seas in climate—A general introduction. *Arctic–Subarctic Ocean Fluxes*, B. Dickson, J. Meincke, and P. Rhines, Eds., Springer, 1–13.
- Good, S. A., M. J. Martin, and N. A. Rayner, 2013: EN4: Quality controlled ocean temperature and salinity profiles and monthly objective analyses with uncertainty estimates. *J. Geophys. Res. Oceans*, **118**, 6704–6716, <https://doi.org/10.1002/2013JC009067>.
- Hartmann, D. L., and P. Ceppi, 2014: Trends in the CERES dataset, 2000–13: The effects of sea ice and jet shifts and comparison to climate models. *J. Climate*, **27**, 2444–2456, <https://doi.org/10.1175/JCLI-D-13-00411.1>.
- Hersbach, H., and Coauthors, 2018: Operational global reanalysis: Progress, future directions and synergies with NWP. ERA Rep. 27, 63 pp., <https://doi.org/10.21957/tkic6g3wm>.
- Hobbs, W., M. D. Palmer, and D. Monselesan, 2016: An energy conservation analysis of ocean drift in the CMIP5 global coupled models. *J. Climate*, **29**, 1639–1653, <https://doi.org/10.1175/JCLI-D-15-0477.1>.
- Kobayashi, S., and Coauthors, 2015: The JRA-55 reanalysis: General specifications and basic characteristics. *J. Meteor. Soc. Japan*, **93**, 5–48, <https://doi.org/10.2151/jmsj.2015-001>.
- Kwok, R., G. F. Cunningham, M. Wensnahan, I. Rigor, H. J. Zwally, and D. Yi, 2009: Thinning and volume loss of the Arctic Ocean sea ice cover: 2003–2008. *J. Geophys. Res. Oceans*, **114**, C07005, <https://doi.org/10.1029/2009JC005312>.
- Lindsay, R. W., and J. Zhang, 2006: Assimilation of ice concentration in an ice-ocean model. *J. Atmos. Oceanic Technol.*, **23**, 742–749, <https://doi.org/10.1175/JTECH1871.1>.
- Liu, C., and Coauthors, 2015: Combining satellite observations and reanalysis energy transports to estimate global net surface energy fluxes 1985–2012. *J. Geophys. Res. Atmos.*, **120**, 9374–9389, <https://doi.org/10.1002/2015JD023264>.
- Llovel, W., J. K. Willis, F. W. Landerer, and I. Fukumori, 2014: Deep-ocean contribution to sea level and energy budget not detectable over the past decade. *Nat. Climate Change*, **4**, 1031–1035, <https://doi.org/10.1038/nclimate2387>.
- Loeb, N. G., B. A. Wielicki, D. R. Doelling, G. L. Smith, D. F. Keyes, S. Kato, N. Manalo-Smith, and T. Wong, 2009: Toward optimal closure of the Earth’s top-of-atmosphere radiation budget. *J. Climate*, **22**, 748–766, <https://doi.org/10.1175/2008JCLI2637.1>.
- , and Coauthors, 2018: Clouds and the Earth’s Radiant Energy System (CERES) energy balanced and filled (EBAF) top-of-atmosphere (TOA) edition-4.0 data product. *J. Climate*, **31**, 895–918, <https://doi.org/10.1175/JCLI-D-17-0208.1>.
- Mayer, M., and L. Haimberger, 2012: Poleward atmospheric energy transports and their variability as evaluated from ECMWF reanalysis data. *J. Climate*, **25**, 734–752, <https://doi.org/10.1175/JCLI-D-11-00202.1>.
- , —, and M. A. Balmaseda, 2014: On the energy exchange between tropical ocean basins related to ENSO. *J. Climate*, **27**, 6393–6403, <https://doi.org/10.1175/JCLI-D-14-00123.1>.
- , —, M. Pietschnig, and A. Storto, 2016: Facets of Arctic energy accumulation based on observations and reanalyses 2000–2015. *Geophys. Res. Lett.*, **43**, 10 420–10 429, <https://doi.org/10.1002/2016GL070557>.
- , —, J. M. Edwards, and P. Hyder, 2017: Toward consistent diagnostics of the coupled atmosphere and ocean energy budgets. *J. Climate*, **30**, 9225–9246, <https://doi.org/10.1175/JCLI-D-17-0137.1>.
- , M. A. Balmaseda, and L. Haimberger, 2018: Unprecedented 2015/16 Indo-Pacific heat transfer speeds up tropical Pacific heat recharge. *Geophys. Res. Lett.*, **45**, 3274–3284, <https://doi.org/10.1002/2018GL077106>.
- Moore, G. W. K., I. A. Renfrew, and R. S. Pickart, 2012: Spatial distribution of air–sea heat fluxes over the sub-polar North Atlantic Ocean. *Geophys. Res. Lett.*, **39**, L18806, <https://doi.org/10.1029/2012GL053097>.
- , K. Våge, R. S. Pickart, and I. A. Renfrew, 2015: Decreasing intensity of open-ocean convection in the Greenland and Iceland seas. *Nat. Climate Change*, **5**, 877–882, <https://doi.org/10.1038/nclimate2688>.
- Mu, L., Q. Yang, M. Losch, S. N. Losa, R. Ricker, L. Nerger, and X. Liang, 2018: Improving sea ice thickness estimates by assimilating CryoSat-2 and SMOS sea ice thickness data simultaneously. *Quart. J. Roy. Meteor. Soc.*, **144**, 529–538, <https://doi.org/10.1002/qj.3225>.
- Nakamura, N., and A. H. Oort, 1988: Atmospheric heat budgets of the polar regions. *J. Geophys. Res.*, **93**, 9510–9524, <https://doi.org/10.1029/JD093iD08p09510>.
- Overland, J. E., and P. Turet, 1994: Variability of the atmospheric energy flux across 70°N computed from the GFDL data set. *The Polar Oceans and Their Role in Shaping the Global Environment*, *Geophys. Monogr.*, Vol. 85, Amer. Geophys. Union, 313–325, <https://doi.org/10.1029/GM085P0313>.
- Peixoto, J. P., and A. H. Oort, 1992: *Physics of Climate*. American Institute of Physics, 520 pp.
- Pietschnig, M., 2016: Volume and energy fluxes in the Arctic Ocean: A comparison between an ocean reanalysis and in-situ observations. Master’s thesis, Faculty of Earth Sciences, Geography and Astronomy, University of Vienna, 97 pp., <http://othes.univie.ac.at/44602/1/46818.pdf>.
- , M. Mayer, T. Tsubouchi, A. Storto, S. Stichelberger, and L. Haimberger, 2018: Volume transports and temperature distributions in the main Arctic gateways: A comparative study between an ocean reanalysis and mooring-derived

- data. EarthArXiv, 35 pp., <https://doi.org/10.31223/OSF.IO/5HG3Z>.
- Porter, D. F., J. J. Cassano, M. C. Serreze, and D. N. Kindig, 2010: New estimates of the large-scale Arctic atmospheric energy budget. *J. Geophys. Res.*, **115**, D08108, <https://doi.org/10.1029/2009JD012653>.
- Ricker, R., S. Hendricks, L. Kaleschke, X. Tian-Kunze, J. King, and C. Haas, 2017: A weekly Arctic sea-ice thickness data record from merged CryoSat-2 and SMOS satellite data. *Cryosphere*, **11**, 1607–1623, <https://doi.org/10.5194/tc-11-1607-2017>.
- Riser, S. C., and Coauthors, 2016: Fifteen years of ocean observations with the global Argo array. *Nat. Climate Change*, **6**, 145–153, <https://doi.org/10.1038/nclimate2872>.
- Robson, J., R. Sutton, K. Lohmann, D. Smith, and M. D. Palmer, 2012: Causes of the rapid warming of the North Atlantic Ocean in the mid-1990s. *J. Climate*, **25**, 4116–4134, <https://doi.org/10.1175/JCLI-D-11-00443.1>.
- Schweiger, A., R. Lindsay, J. Zhang, M. Steele, H. Stern, and R. Kwok, 2011: Uncertainty in modeled Arctic sea ice volume. *J. Geophys. Res.*, **116**, C00D06, <https://doi.org/10.1029/2011JC007084>.
- Semmler, T., D. Jacob, K. H. Schlünzen, and R. Podzun, 2005: The water and energy budget of the Arctic atmosphere. *J. Climate*, **18**, 2515–2530, <https://doi.org/10.1175/JCLI3414.1>.
- Sen, P. K., 1968: Estimates of the regression coefficient based on Kendall's tau. *J. Amer. Stat. Assoc.*, **63**, 1379–1389, <https://doi.org/10.1080/01621459.1968.10480934>.
- Serreze, M. C., and R. G. Barry, 2011: Processes and impacts of Arctic amplification: A research synthesis. *Global Planet. Change*, **77**, 85–96, <https://doi.org/10.1016/j.gloplacha.2011.03.004>.
- , and —, 2014: *The Arctic Climate System*. Cambridge University Press, 415 pp.
- , A. P. Barrett, A. G. Slater, M. Steele, J. Zhang, and K. E. Trenberth, 2007: The large-scale energy budget of the Arctic. *J. Geophys. Res.*, **112**, D11122, <https://doi.org/10.1029/2006JD008230>.
- Simmons, A. J., and D. M. Burridge, 1981: An energy and angular-momentum conserving vertical finite-difference scheme and hybrid vertical coordinates. *Mon. Wea. Rev.*, **109**, 758–766, [https://doi.org/10.1175/1520-0493\(1981\)109<0758:AEAAMC>2.0.CO;2](https://doi.org/10.1175/1520-0493(1981)109<0758:AEAAMC>2.0.CO;2).
- Steele, M., J. Zhang, and W. Ermold, 2010: Mechanisms of summertime upper Arctic Ocean warming and the effect on sea ice melt. *J. Geophys. Res.*, **115**, C11004, <https://doi.org/10.1029/2009JC005849>.
- Storto, A., and S. Masina, 2016: C-GLORSv5: An improved multipurpose global ocean eddy-permitting physical reanalysis. *Earth Syst. Sci. Data*, **8**, 679–696, <https://doi.org/10.5194/essd-8-679-2016>.
- , and Coauthors, 2019: Ocean reanalyses: Recent advances and unsolved challenges. *Front. Mar. Sci.*, **6**, 418, <https://doi.org/10.3389/fmars.2019.00418>.
- Tietsche, S., D. Notz, J. H. Jungclauss, and J. Marotzke, 2013: Assimilation of sea-ice concentration in a global climate model—Physical and statistical aspects. *Ocean Sci.*, **9**, 19–36, <https://doi.org/10.5194/os-9-19-2013>.
- , M. Alonso-Balmaseda, H. Zuo, and K. Mogensen, 2014: Arctic sea ice in the ECMWF MyOcean2 ocean reanalysis ORAP5. ECMWF Tech. Memo. 737, 33 pp., <https://doi.org/10.21957/i9s4wt41>.
- , —, P. Rosnay, H. Zuo, X. Tian-Kunze, and L. Kaleschke, 2018: Thin Arctic sea ice in L-band observations and an ocean reanalysis. *Cryosphere*, **12**, 2051–2072, <https://doi.org/10.5194/tc-12-2051-2018>.
- Toole, J. M., R. A. Krishfield, M.-L. Timmermans, and A. Proshutinsky, 2011: The ice-tethered profiler: Argo of the Arctic. *Oceanography*, **24**, 126–135, <https://doi.org/10.5670/OCEANOGRAPHY.2011.64>.
- Tsubouchi, T., and Coauthors, 2018: The Arctic Ocean seasonal cycles of heat and freshwater fluxes: Observation-based inverse estimates. *J. Phys. Oceanogr.*, **48**, 2029–2055, <https://doi.org/10.1175/JPO-D-17-0239.1>.
- Uotila, P., and Coauthors, 2019: An assessment of ten ocean reanalyses in the polar regions. *Climate Dyn.*, **52**, 1613–1650, <https://doi.org/10.1007/s00382-018-4242-z>.
- Uppala, S. M., and Coauthors, 2005: The ERA-40 re-analysis. *Quart. J. Roy. Meteor. Soc.*, **131**, 2961–3012, <https://doi.org/10.1256/qj.04.176>.
- von Schuckmann, K., and Coauthors, 2016: An imperative to monitor Earth's energy imbalance. *Nat. Climate Change*, **6**, 138–144, <https://doi.org/10.1038/nclimate2876>.
- , and Coauthors, 2018: Copernicus Marine Service Ocean State Report. *J. Oper. Oceanogr.*, **11**, S1–S142, <http://marine.copernicus.eu/science-learning/ocean-state-report/ocean-state-report-2nd-issue/>.
- Wielicki, B. A., B. R. Barkstrom, E. F. Harrison, R. B. Lee, G. L. Smith, and J. E. Cooper, 1996: Clouds and the Earth's Radiant Energy System (CERES): An Earth Observing System Experiment. *Bull. Amer. Meteor. Soc.*, **77**, 853–868, [https://doi.org/10.1175/1520-0477\(1996\)077<0853:CATERE>2.0.CO;2](https://doi.org/10.1175/1520-0477(1996)077<0853:CATERE>2.0.CO;2).
- Zuo, H., M. A. Balmaseda, S. Tietsche, K. Mogensen, and M. Mayer, 2019: The ECMWF operational ensemble reanalysis-analysis system for ocean and sea-ice: A description of the system and assessment. *Ocean Sci.*, **15**, 779–808, <https://doi.org/10.5194/os-15-779-2019>.
- Zwally, H. J., D. Yi, R. Kwok, and Y. Zhao, 2008: ICESat measurements of sea ice freeboard and estimates of sea ice thickness in the Weddell Sea. *J. Geophys. Res.*, **113**, C02S15, <https://doi.org/10.1029/2007JC004284>.